Invited Comment

Multiscale modeling and nested simulations of three-dimensional ionospheric plasmas: Rayleigh–Taylor turbulence and nonequilibrium layer dynamics at fine scales

Alex Mahalov[1]

Arizona State University, Tempe, AZ 85287-1804, USA

E-mail: mahalov@asu.edu

Abstract

Multiscale modeling and high resolution three-dimensional simulations of nonequilibrium ionospheric dynamics are major frontiers in the field of space sciences. The latest developments in fast computational algorithms and novel numerical methods have advanced reliable forecasting of ionospheric environments at fine scales. These new capabilities include improved physics-based predictive modeling, nesting and implicit relaxation techniques that are designed to integrate models of disparate scales. A range of scales, from mesoscale to ionospheric microscale, are included in a 3D modeling framework. Analyses and simulations of primary and secondary Rayleigh–Taylor instabilities in the equatorial spread F (ESF), the response of the plasma density to the neutral turbulent dynamics, and wave breaking in the lower region of the ionosphere and nonequilibrium layer dynamics at fine scales are presented for coupled systems (ions, electrons and neutral winds), thus enabling studies of mesoscale/microscale dynamics for a range of altitudes that encompass the ionospheric E and F layers. We examine the organizing mixing patterns for plasma flows, which occur due to polarized gravity wave excitations in the neutral field, using Lagrangian coherent structures (LCS). LCS objectively depict the flow topology and the extracted scintillation-producing irregularities that indicate a generation of ionospheric density gradients, due to the accumulation of plasma. The scintillation effects in propagation, through strongly inhomogeneous ionospheric media, are induced by trapping electromagnetic (EM) waves in parabolic cavities, which are created by the refractive index gradients along the propagation paths.

Keywords: plasma dynamics, ionospheric layers, Rayleigh–Taylor instabilities, nested simulations

1. Introduction

Turbulent hydrodynamic mixing, induced by Rayleigh–Taylor (RT) instabilities, occurs in settings that are as varied as exploding stars (supernovae), inertial confinement fusion (ICF) and macroscopic flows in fluid dynamics, such as ionospheric plasmas ([1–4, 11, 58, 95, 99, 100, 122]). Since

the discovery of the plasma instability phenomenon that occurs in the nighttime equatorial F-region ionosphere, which is revealed by rising plumes that are identified as large-scale depletions or bubbles, considerable efforts have been made in the development of computer models that simulate the generation and evolution of the Equatorial Spread F (ESF) dynamics ([9, 11, 17, 29, 30, 41, 49, 58, 75, 76, 83–85, 87, 89, 99, 100, 104, 110]). The book by M C Kelley [50], contains a comprehensive list of references to 2009.

---

[1] The Wilhoit Foundation Dean's Distinguished Professor.

The ionosphere is a dynamic mixture of ions, electrons and neutral gases, surrounding the Earth in the altitude range of approximately 90 km to beyond 1000 km. The ionosphere can also be viewed as a transition region from the Earth's lower atmospheric regions (i.e., the troposphere, stratosphere and mesosphere) to the outer space environment (i.e., the magnetosphere). As such, the ionosphere acts to mediate and transmit external forces and drivers from below and above. Understanding and modeling the ionosphere is a daunting but important challenge because of its critical role in space sciences. Significant progress has been made in the development of computational models of the ionosphere over the past several decades. However, the current modeling capabilities need further development, especially with regard to coupling the physical processes that occur over a large range of temporal and spatial scales that characterize the ionosphere. In particular, advances are needed in the ability to make accurate high resolution forecasts over limited-area ionospheric environments, which are required for operational communication, navigation and imaging applications.

The ionosphere involves interactions between phenomena of varying scale sizes ([6, 12, 19–21, 26, 33–34, 36–41, 46, 48, 52, 53, 72, 77–90, 96–122]). Large-scale variations, like the solar cycle, seasonal effects and tidal effects, all drive large-scale changes in the global structure. Such changes define the mean state (climate) of the ionospheric system. These processes have characteristic spatial scales greater than a thousand kilometers and time scales that range from several hours to a few years. General circulation models have been developed to simulate these large-scale structures (e.g., [14, 18, 22, 23, 47, 48 86]). These global models, together with the large observational data sets that have been accumulated over the years, have led to a much greater understanding of large-scale structures in the ionosphere and to the response of these structures to variations in geophysical inputs. Space weather is the perturbation of the ionosphere and the thermosphere from its long-term global mean state. These perturbations involve not only large-scale variations, but also mesoscale and small-scale processes that occur locally and may have short periods. Mesoscale and small-scale processes, such as auroral arcs and the mid-latitude electron density trough, affect not only local plasma and neutral distributions but also large-scale structures through dynamical and energetic coupling. Such couplings between processes of different scales occur in the equatorial region and in the mid-latitudes and high latitudes. The dynamics of large and mesoscale neutral winds are often characterized by the presence of zonal jets and anisotropic turbulence, i.e. [24], and [13]. Improving our understanding of neutral/plasma interactions at ionospheric meso/microscales is a challenge for ionospheric science studies. M C Kelley ([50], p. 456) states, 'we simply do not understand neutral/plasma interactions on our own planet.' Current models are limited because of their use of empirical models of the ionosphere for prescribed neutral conditions, which decouple the dynamics of neutral and charged particles. They are also limited by the assumption of neglecting the inertial terms and by imposing isothermal conditions for both charged and neutral species.

The electron density in the ionosphere varies diurnally, geographically, seasonally and with the Sunspot number, along with other solar phenomena. The total electron content (TEC) can vary by two orders of magnitude, depending on the time and the location of the observations. Apart from the variation with altitude, the electron density varies with the activity level of the Sun, the time of the year, the time of the day and the geographical position. In addition, a number of stochastic effects and scintillations play an important role in the influence of the ionosphere on electromagnetic wave propagation. At low latitude, an important scintillation source is F-spread. F-spread is caused by rod-shaped magnetic field-aligned bubbles, which are formed in the F-layer just after sunset and have a lifetime of 2–3 h. The edges of the F-spread bubbles are highly unstable and can be the source of intensity scintillations. F-spread is more prevalent during equinoxes and summers, occurs preferentially during magnetically quiet periods and increases with increasing sun activity. At high latitude, the aurora can cause severe distortions of the electromagnetic (EM) waveforms. The aurora is the result of high-energy electrons from the solar wind, which, at polar regions, can sometimes break through the barrier of the Earth's magnetic field. These electrons ionize atoms and therefore cause the electron density to increase.

For the study of multiscale ionospheric dynamics over a limited spatial range in latitude, longitude and altitude, nested coupled mesoscale/microscale models need to be created and used in order to generate high resolution data, which is then used to produce accurate predictions and forecasts. The challenge of multiscale nesting and High Performance Computing (HPC) simulations for the dynamically evolving limited-area ionospheric environments is to achieve the robust predictability and ensemble forecasting of high-impact ionospheric events. Furthermore, these high resolution regions need to be resolved even further by coupling to advanced fluid, hybrid, and/or Lagrangian particle tracking codes, which provide the necessary physics to study ionospheric processes at fine scales. This is a daunting but important challenge to meet. Significant advances in the computation of atmospheric and environmental flows at lower atmospheric levels have been achieved during the last decade. A dramatic increase in computer power has facilitated the development of numerical codes that have the capability to resolve small-scale atmospheric processes. This was achieved by the implementation of fast computational algorithms and nesting techniques with multiple domains that resolve fine horizontal and vertical scales and by the improvement of physics-based predictive modeling for shear-stratified flows in the upper troposphere and lower stratosphere ([43, 59, 60]). Multiscale modeling of the Earth's ionosphere has, however, received less attention compared to lower atmospheric levels, and it remains one of the major frontiers of space sciences. One of the main difficulties researchers face in the development of a nested modeling approach for ionospheric equations is the specification of the boundary conditions. Additional complications in the computations of ionospheric flows arise from the equation for the electric potential, which is a diagnostic variable computed from nonlinear elliptic equations.

In this review, we describe a novel multiscale modeling approach, or nesting, to capture fine-scale ionospheric dynamics, in which models that are able to resolve different scales are coupled. The prognostic fields at the boundaries of the nested model are specified from a large-scale model. The large domain model, with a coarse resolution, is used to predict large-scale structures, while a limited domain (or nested) model with boundary conditions interpolated from the coarse grid (or parent) model is used over smaller domains with finer resolutions. Small-scale structures, which are not resolved in the coarse grid model and therefore need to be represented by some kind of parameterization, are explicitly resolved in the nested model; this is the improvement achieved by this approach. This methodology was applied, with success, to the multiscale resolution of the atmospheric flows in the upper troposphere and lower stratosphere ([43, 59–66]). The extension of multi-nested computational methods to the ionosphere presents significant challenges, as the presence of ions and electrons increases the complexity of the model equations.

Here, we present high resolution multiscale nested simulations of ionospheric dynamics, in which nested fields are relaxed toward large domain fields. We describe a new multiscale computational method based on the flow relaxation scheme, in which the relaxation is implemented as an implicit correction ([59]). We show examples that demonstrate that this method is very effective and robust in the context of ionospheric flows. Computational results in real ionospheric Equatorial Spread F (ESF) conditions are presented, which demonstrate the ability of the proposed nested approach to resolve the multiscale physics of strongly nonlinear structures observed in the ESF and to improve the resolution of the primary and secondary ionospheric Rayleigh–Taylor (RT) instabilities and non-equilibrium plasma dynamics ([58, 99, 100]). We examine the organizing mixing patterns for the plasma flows due to polarized gravity wave excitations in the neutral field, using Lagrangian coherent structures (LCS). LCS objectively depict the flow topology, and the extracted scintillation producing irregularities indicate a generation of ionospheric density gradients due to the accumulation of plasma. The scintillation effects are induced by trapping electromagnetic (EM) waves in parabolic cavities, created by the refractive index gradients along the propagation paths ([54, 57, 68]).

This paper is organized as follows. The model formulation and the computational approach are presented in section 2. The performance and the ability of the nested simulations to resolve small-scale structures associated with Rayleigh–Taylor instabilities and the ESF are demonstrated in section 3. In section 4, our studies focus on the charge-neutral interactions and the associated stochastic Lagrangian dynamics. In particular, we examine the organizing mixing patterns for plasma flows due to polarized gravity wave excitations in the neutral field, using Lagrangian coherent structures (LCS) methods. Finally, the summary and challenges are discussed in section 5.

2. Multiscale coupled mesoscale/microscale limited-area ionospheric models: nesting and implicit relaxation computational techniques

2.1. Governing equations

The three–dimensional equations for ionospheric dynamics include the coupling of the neutral fluid, the ion gas, the electron gas and the electromagnetic equations ([50, 88]).

2.1.1. Equations for the neutral fluid.

$$\frac{\partial \rho}{\partial t} + \vec{V} \cdot \vec{U} = 0$$

$$\frac{\partial U}{\partial t} + \vec{V} \cdot \left(\vec{U} u \right) + \frac{\partial p}{\partial x} + \left(2\vec{\Omega} \times \vec{U} - \vec{J} \times \vec{B} \right)_x = F_U$$

$$\frac{\partial V}{\partial t} + \vec{V} \cdot \left(\vec{U} v \right) + \frac{\partial p}{\partial y} + \left(2\vec{\Omega} \times \vec{U} - \vec{J} \times \vec{B} \right)_y = F_V$$

$$\frac{\partial W}{\partial t} + \vec{V} \cdot \left(\vec{U} w \right) + \frac{\partial p}{\partial z} - \rho g + \left(2\vec{\Omega} \times \vec{U} - \vec{J} \times \vec{B} \right)_z = F_W$$

$$\frac{\partial \Theta}{\partial t} + \vec{V} \cdot \left(\vec{U} \theta \right) = F_\theta$$

$$p = \rho k_b T / m = n k_b T$$

$$\theta = \frac{p}{\rho^\gamma}.$$

In these equations, $\vec{U} = (U, V, W)$ is the coupled velocity $(\vec{U} = \rho \vec{u})$, $\vec{u} = (u, v, w)$ is the physical velocity vector, $\vec{\Omega}$ is the Earth's rotation, $\vec{J}$ is the density current of the charged particles (ions and electrons), $\vec{B}$ is the Earth magnetic field vector, T is the temperature, θ is conserved for adiabatic motion and Θ is its coupled variable ($\Theta = \rho \theta$). p is the pressure, ρ is the density, $\vec{g}$ is the acceleration of gravity vector, m is the mass, n is the number density and k_b is Boltzmann's constant. The right-hand side terms F_U, F_V, F_W and F_θ represent forcing terms that arise from model physics, turbulent mixing and heating.

The above equations for neutrals are coupled with equations for the charged fluid, which include ion and electron gases.

2.1.2. Equations for the ion gas.

$$\frac{\partial n_i}{\partial t} + \vec{V} \cdot \left(n_i \vec{v}_i \right) = P_i - L_i$$

$$\rho_i \frac{d\vec{v}_i}{dt} = n_i e \left(\vec{E} + \vec{v}_i \times \vec{B} \right) + n_i m_i \vec{g} - \vec{V} p_i + n_i m_i \nu_{in} \left(\vec{u} - \vec{v}_i \right)$$

$$\frac{\partial T_i}{\partial t} + \vec{v}_i \cdot \vec{V} T_i + \frac{2}{3} T_i \vec{V} \cdot \vec{v}_i - \frac{2}{3} \frac{1}{n_i k_b} b_s^2 \frac{\partial}{\partial s} \left(\kappa_i \frac{\partial T_i}{\partial s} \right)$$

$$= Q_{in} + Q_{ii} + Q_{ie}$$

$$p_i = n_i k_b T_i.$$

In these equations, $\vec{v}_i$ is the ion velocity vector, $\vec{E}$ is the electric field vector, T_i is the temperature, p_i is the pressure, n_i is the number density of ion, $\vec{g}$ is the acceleration of the gravity vector, κ_i is the thermal conductivity and ν_{in} is the collision frequency of the ions with the neutrals. Here, $b_s = \frac{B}{B_0}$, where B is the geomagnetic dipole field, and B_0 is
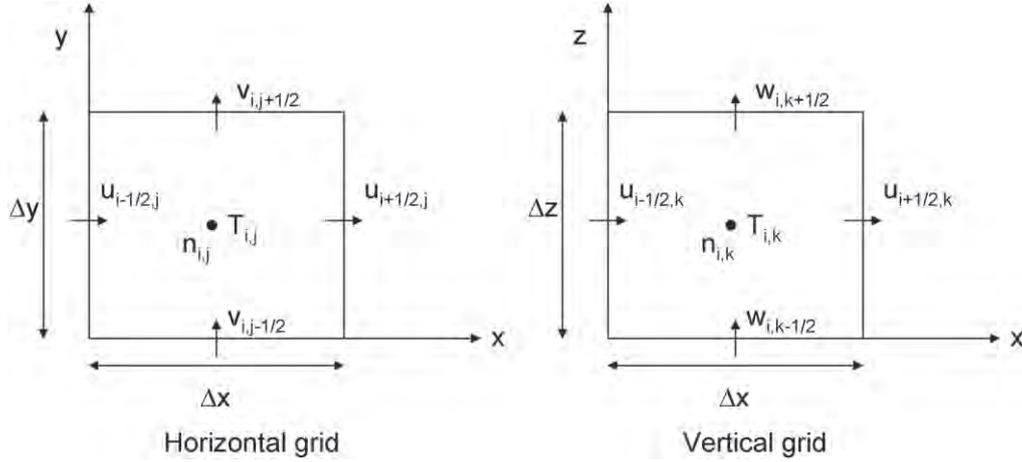
Figure 1. Horizontal and vertical cells of the C grid staggering.

its value at the Earth's surface, and s is the coordinate along the magnetic field lines. The right-hand side terms P_i and L_i represent the production and loss coefficients of the ion gas. Q_{in}, Q_{ii} and Q_{ie} represent the heating terms, which are due to ion-neutral collisions, ion-ion collisions and ion-electron collisions, respectively.

2.1.3. Equations for the electron gas.

$$n_e = \sum_i n_i$$

$$\rho_e \frac{d\vec{v}_e}{dt} = -n_e e(\vec{E} + \vec{v}_e \times \vec{B}) + n_e m_e \vec{g}$$
$$- \nabla p_e + n_e m_e \nu_{en}(\vec{u} - \vec{v}_e)$$

$$\frac{\partial T_e}{\partial t} - \frac{2}{3}\frac{1}{n_e k_b}b_s^2\frac{\partial}{\partial s}\left(\kappa_e \frac{\partial T_e}{\partial s}\right) = Q_{en} + Q_{ei} + Q_{phe}$$

$$p_e = n_e k_b T_e$$

In these equations, $\vec{v}_e$ is the electron velocity vector, $\vec{E}$ is the electric field vector, T_e is the temperature of the electron gas, p_e is the pressure, n_e is the number density of the electron, $\vec{g}$ is the acceleration of the gravity vector, κ_e is the thermal conductivity for electrons and ν_{en} is the collision frequency of the electrons with the neutrals. Q_{en} and Q_{ei} represent the heating terms, which are due to the electron-neutral collisions and to the electron-ion collisions, respectively. Q_{phe} is due to photoelectron heating.

2.1.4. Electromagnetic equations.

$$\vec{J} = \sum_j n_j q_j \vec{v}_j = e\left(\sum_i n_i \vec{v}_i - n_e \vec{v}_e\right)$$

$$\vec{\nabla} \cdot \vec{J} = 0$$

$$\vec{J} = \sigma \bullet \left(\vec{E} + \vec{u} \times \vec{B}\right)$$

$$\vec{E} = -\nabla \varphi.$$

In these equations, $\vec{J}$ is the density current, $\vec{E}$ is the electric field vector, ϕ is the electric potential, σ is the conductivity tensor, e is the charge of the electron and q_j is the charge of the jth species. The electric field vector ($\vec{E}$) and the potential ϕ are calculated so that the relation $\vec{\nabla} \cdot \vec{J} = 0$ is satisfied.

In order to characterize multiscale ionospheric dynamics over a limited spatial range in the latitude, longitude and altitude, we use nested coupled mesoscale/microscale models to generate high resolution data, which is used to produce accurate predictions and forecasts. Our typical limit area high resolution simulations focus on a 3D ionospheric domain, which is centered on a geographical region that spans several hundred kilometers horizontally and encompasses altitudes from 80 km to 500 km. Nested capabilities allow selected time intervals and spatial locations to run at a higher resolution. The smallest mesoscale domains are typically about 300 km × 300 km horizontally in the ionosphere; the embedded microscale domains are 100 km × 100 km or finer and are zoomed on altitudes that encompass the ionospheric E-F layers. Running global models with comparable fine resolution in order to resolve ionospheric meso/microscale dynamics in targeted regions is prohibitive due to the computational costs.

2.2. Model numerics

The solver for neutral and charged gases uses a time-split integration scheme. Slow or low-frequency modes are integrated using a third-order Runge Kutta (RK3) time integration scheme, while the high-frequency modes are integrated over smaller time steps in order to maintain numerical stability. The horizontally propagating acoustic modes and fast waves are integrated using a forward-backward time integration scheme, and vertically propagating acoustic modes are integrated using a vertically implicit scheme (using the acoustic time step). This time-splitting is similar to what is described in the atmospheric codes and analyzed in [60, 92]. The acoustic-mode integration is cast in the form of a correction to the RK3 integration. The RK3 scheme integrates a set of partial differential equations by using a predictor-corrector formulation. The high-frequency acoustic modes would severely limit the RK3 time step. We use the time-split approach in order to circumvent this time step limitation.

Additionally, to increase the accuracy of the splitting, we integrate a perturbation form of the governing equations by using smaller acoustic time steps within the RK3 large-time-step sequence. To form the perturbation equations for the RK3 time-split acoustic integration, we define small time step variables that are deviations from the most recent RK3 predictor $\left(\psi'' = \psi - \psi^t\right)$.

The spatial discretization in the solver uses C grid staggering for the variables, as shown in figure 1. That is, normal velocities are staggered one-half grid length from the thermodynamic variables. The variable indices (i, j, k) indicate variable locations. We denote the points where the density is located as thermodynamic points, and likewise, we denote the locations where u, v, and w are defined as u points, v points and w points, respectively. The mass and the number density for neutrals, ions and electrons are defined at the (i, j, k) points. The pressure p is computed at the thermodynamic points. The grid spacing Δx and Δy are constants in the model formulation. The vertical grid spacing Δz is not a fixed constant; it is specified in the initialization.

The RK3 advection uses a third order in the vertical accurate spatial discretizations and a fifth order in the horizontal accurate spatial discretizations of the flux divergence for momentum, scalars and temperature, using the RK3 time-integration scheme. The formulation of the odd-order schemes are comprised of the next higher (even) order centered scheme, plus an upwind term that, for a constant transport mass flux, is a diffusion term of that next higher (even) order with a hyper-viscosity that is proportional to the Courant number. The diffusion term is the leading order error term in the flux divergence discretization. The Positive-Definite Limiter for the RK3 advection of charged and neutral chemical species or other tracer species should remain positive definite; that is, negative masses should not be permitted. The Runge-Kutta transport integration, defined by the time stepping algorithm and combined with the flux divergence operator, is conservative, but it does not guarantee positive definiteness. Any negative values are offset by the positive mass, such that the mass is conserved. In many physics options, negative concentrations and densities are set to zero, which results in an increase in the mass of that species. A positive-definite flux renormalization, applied on the final Runge-Kutta transport step, can be used to remove this unphysical effect from the RK3 scalar transport scheme. The model is typically integrated with a fixed time step, which is chosen to produce a stable integration. During any time in the integration, the maximum stable time step is likely to be larger than the fixed time step. An adaptive time stepping capability is introduced so that the RK3 time step can be chosen based on the temporally evolving wind fields. The adaptively chosen time step is usually larger than the typical fixed time step; hence, the dynamics integrate faster, and the physics parameterizations are called less often. Also, the time-to-completion of the simulation can be substantially reduced.

Recently, a fast time stepping method, based on leapfrog and a new high order implicit time filter, was developed in [73]. The amplitude errors in this scheme are of the third order, which is comparable to the amplitude errors of the third order RK scheme. The new scheme, however, only requires one function evaluation per time step as opposed to the RK3 time step, which is more expensive since it requires three evaluations for each time step (the new scheme is three times faster than the currently used schemes and incorporates the same level of accuracy). This makes the numerical method in [73] a potential alternative for applications in high resolution computational modeling and in the forecasting of ionospheric dynamics.

2.3. Multi-Nesting

In the study of limited-area ionospheric environments, one key challenge is the development of nesting methods that use robust computational techniques to control numerical errors, such as the ones that are generated at the boundaries of the nested models. These errors are inevitable in any nested or downscaled simulation because the coarse grid fields that are specified at the boundaries of the nested grid are not consistent with the finer fields that are simulated by the nest. If not treated effectively, these errors will propagate into the interior of the nested domain, thereby resulting in the poor quality of the numerical simulations. These errors are particularly important when instabilities dominate the dynamics near the boundaries of the nested domain. Thus, numerical methods that control and reduce the propagation of these errors are essential for reliable high resolution regional predictions in the ionosphere.

There are two main techniques that are used in atmospheric and oceanic downscaling models to improve resolution over limited areas. In dynamically adaptive methods, the spatial resolution constantly changes with time by coarsening or refining the grid spacing, depending on the local conditions ([8, 15]). The adaptive methods are not well-established in the atmospheric modeling systems for several reasons ([8]): (i) adaptive techniques can incur massive overhead due to indirect data addressing and to the additional efforts needed for grid handling, which increase the cost of the real-time forecasting or the long-term predictions; (ii) physical parameterizations of subgrid processes are usually optimized for a specific grid resolution, which makes it difficult to use dynamically and temporally refined or coarsened grids. An important class of numerical methods uses nesting to improve spatial resolution over a limited area. Nesting techniques are widely used in atmospheric ([42, 59, 60, 64, 66, 92–94]) and oceanic ([28, 91]) models. Large domain models with coarse resolution are used to predict large-scale dynamics, while limited-area models with boundary conditions that are interpolated from coarse grids are used over embedded domains with a finer resolution. Small-scale processes, which are not resolved in a coarse grid model and therefore need to be represented by using subgrid-scale parameterizations, may be explicitly resolved in the nested model; this is the improvement achieved by nesting techniques.

The horizontal and vertical nesting capabilities allow the resolution to be focused over a region of interest in the ionosphere by introducing an additional grid (or grids) into the simulation. Vertical and horizontal refinements are
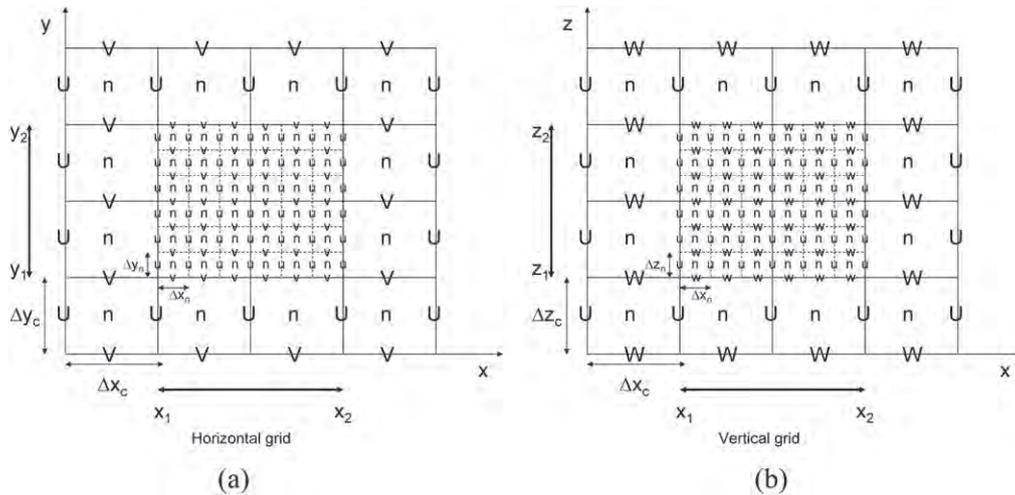
Figure 2. (a) Horizontal Arakawa-C grid staggering for a portion of a parent domain and an imbedded nest domain with a 3:1 grid size ratio. The solid lines denote coarse grid cell boundaries, and the dashed lines are the boundaries for each fine grid cell. The horizontal components of velocity (U and V) are defined along the normal cell face, and the thermodynamic variables n are defined at the center of the grid cell (each square). The variables along the interface between the coarse and the fine grid define the locations where the specified lateral boundaries for the nest are in effect. (b) Vertical Arakawa-C grid staggering for a portion of a parent domain and an imbedded nest domain with a 3:1 grid size ratio. The solid lines denote coarse grid cell boundaries, and the dashed lines are the boundaries for each fine grid cell. The eastward and the vertical components of velocity (U and W) are defined along the normal cell face, and the thermodynamic variables n are defined at the center of the grid cell (each square). The variables along the interface between the coarse and the fine grid define the locations where the specified lateral boundaries for the nest are in effect.

available. The nested grids are rectangular and are aligned with the parent (coarser) grid within which they are nested. Additionally, the nested grids allow any integer spatial and temporal refinement ratios of the parent grid (the spatial and temporal refinement ratios are usually 3, but are not necessarily the same for each nest). This nesting implementation is, in many ways, similar to the implementations in the mesoscale and microscale models in the troposphere and stratosphere; it allows nesting with the embedded nested domains in the horizontal as well as in the vertical directions (figure 2), and it allows a robust novel method to control errors near the boundaries (implicit relaxation).

Nested grid simulations can be produced using either 1-way nesting or 2-way nesting. The 1-way and 2-way nesting options refer to how the coarse grid and the fine grid interact. In both the 1-way and 2-way simulation modes, the fine grid boundary conditions (i.e., the lateral and vertical boundaries) are interpolated from the coarse grid forecast. In a 1-way nest, this is the only information exchange between the grids (from the coarse grid to the fine grid). In the 2-way nest integration, the fine grid solution replaces the coarse grid solution with coarse grid points that lie inside the fine grid. This information exchange between the grids is now in both directions (coarse-to-fine for the fine-grid lateral, bottom and top boundary computation and fine-to-coarse during the feedback at each coarse grid time step). The 1-way nest setup may be run by one of two different methods. One option is to produce the nested simulation as two separate simulations. In this mode, the coarse grid is integrated first, and the coarse grid forecast is completed. Output from the coarse grid integration is then processed in order to provide boundary conditions for the nested run (usually at a much lower temporal frequency than the coarse grid time step); and this is followed by the

complete time integration of the fine (nested) grid. Hence, this 1-way option is equivalent to running two separate simulations with a processing step in between. The second 1-way option (lockstep with no feedback), is run as a traditional simulation with two (or more) grids integrating concurrently, except with the feedback runtime option shut off. This option provides lateral boundary conditions to the fine grid at each coarse grid time step, which is an advantage of the concurrent 1-way method (no feedback).

The model allows the refinement of a coarse-grid simulation along with the introduction of a nested grid. An option for initializing the fine grid is provided when using concurrent 1-way and 2-way nesting. All of the fine grid variables are interpolated from the coarse grid. This option allows the fine grid to start at a later time in the coarse grid's simulation. A simulation involves one outer grid and may contain multiple inner nested grids. Each nested region is entirely contained within a single coarser grid, referred to as the *parent* grid. The finer nested grids are referred to as *child* grids. Using this terminology, children are also parents when multiple levels of nesting are used. The fine grids may be telescoped to any depth (i.e., a parent grid may contain one or more child grids, each of which, in turn, may successively contain one or more child grids), and several fine grids may share the same parent at the same level of nesting. For both 1-way and 2-way nested grid simulations, the ratio of the parent horizontal grid distance to the child horizontal grid distance (the spatial refinement ratio) must be an integer. In the cases of 2-way and concurrent 1-way nesting, this is also true for the time steps (the temporal refinement ratio). The model does allow the time step refinement ratio to differ from the spatial refinement ratio.

The model uses Arakawa-C grid staggering. As shown in figure 1, the u, v and w components of the horizontal velocity

are normal to the respective faces of the grid cell, and the thermodynamic, density and chemistry variables are located in the center of the cell. The variable staggering has an additional column of u in the x-direction, an additional row of v in the y-direction and an additional row of w in the z-direction because the normal velocity points define the grid boundaries. The horizontal momentum components reflect an average across each cell face, while each thermodynamic, density and chemistry variable is the representative mean value throughout the cell. Feedback is handled to preserve these mean values: the thermodynamic, density and chemistry fields are fed back with an average from within the entire coarse grid point, and the horizontal momentum variables are averaged along their respective normal coarse grid cell faces. The horizontal interpolation (to instantiate a grid and to provide time-dependent lateral, bottom and top boundaries) does not conserve mass. The feedback mechanism uses cell averages (for thermodynamic, density and chemistry quantities) and cell-face averages for the horizontal momentum fields. The staggering defines the way that the fine grid is situated on top of the coarse grid. For all odd ratios, there is a coincident point for each variable: a location that has the coarse grid and the fine grid at the same physical point. The location of this point depends on the variable. In each of the coarse grid cells with an odd ratio, the middle fine grid cell is the coincident point with the coarse grid for all of the mass-staggered fields (figure 2). For the horizontal momentum variables, the normal velocity has coincident points along the grid boundaries for odd ratios.

2.4. Implicit relaxation

One of the main difficulties faced in atmospheric as well as oceanic downscaling modeling is the specification of the lateral boundary conditions. Usually, the prognostic fields at the lateral boundaries of the nested grid are specified from the large domain. These fields have coarse resolution, and are interpolated in space and time to the nested grid. The inconsistencies between the limited and the large domain solutions create spurious reflections that may propagate and affect the solution in the interior of the nested domain. Several approaches are used to handle the lateral boundary conditions. The flow relaxation scheme ([10]) is the most frequently used for atmospheric mesoscale forecasting models over a limited domain. Lateral open boundary conditions are often used in limited-area ocean modeling. These conditions include the radiation condition, the combined radiation and prescribed condition, which depends on the inflow and outflow regime at the boundary, and a scale selective approach. A review of these methods is given in [74].

We have developed a novel technique of implicit relaxation for limited-area horizontally and vertically nested ionospheric models, with a particular emphasis on improved vertical resolution for altitudes in the range of 80 km–500 km. The relaxation method consists of progressively relaxing the fine grid fields toward the coarse grid fields. This method is implemented using an operator splitting method that is applied in the acoustic steps, in which a prognostic variable is
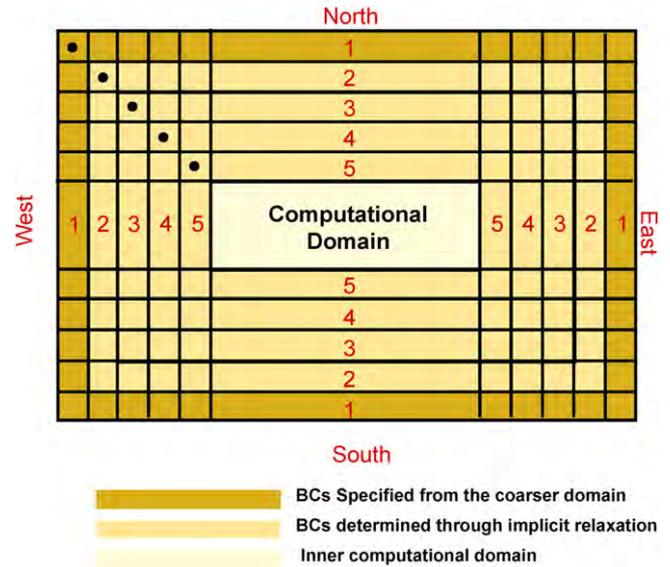

Figure 3. Specified and relaxation zones for a grid with a single specified row and column and four rows and columns for the relaxation zone.

updated first, without any relaxation. The relaxation is applied as an implicit correction step after each acoustic step. The corrected variable is then used to update the other prognostic variables ([58–60, 64, 66, 99, 100]).

For the fine grid with 2-way nesting or 1-way nesting (using a concurrent simulation, see figure 2), the boundary conditions are specified by the parent grid at every coarse grid time step. Prognostic variables are entirely specified in the outer row and in the column of the fine grid through spatial and temporal interpolation from the coarse grid (the coarse grid is stepped forward in time prior to the advancement of any child grid of that parent). The nested boundary condition is also referred to as a relaxation, or nudging, boundary condition. The nested grid's lateral and vertical boundaries are comprised of both a specified zone and a relaxation zone, as shown in figure 3. For the coarse grid, the specified zone is determined entirely by temporal interpolation from the coarse grid. The last row and column along the outer edge of the nested grid is entirely specified by temporal interpolation, using data from the coarse grid. The second region of the lateral boundary for the coarse grid is the relaxation zone. The relaxation zone is where the model is nudged or relaxed towards the larger-scale field (e.g., rows and columns 2 through 5 in figure 3). The size of the relaxation zone can be adjusted to any number.

The normal velocity component that is located at the boundary (u point, v point and w point) is treated differently than the tangential velocities and the thermodynamic variables, which are located one-half grid point inside the domain and are adjacent to the boundary. The relaxation boundary scheme involves smoothly constraining the main prognostic variables of the nested model to match the corresponding values from the coarse grid model in a buffer zone next to the boundary called the 'relaxation' zone. The flow relaxation scheme is a combination of Newtonian and diffusive

relaxation, and has the form:

$$\partial_t \psi = -N(x)\left(\psi - \psi^c\right) + D(x)\partial_{xx}\left(\psi - \psi^c\right)$$

where ψ is a prognostic variable of the limited-area model that needs to be relaxed to the corresponding variable from the coarse grid model ψ^c, x denotes the direction normal to the boundary and $N(x)$ and $D(x)$ are the Newtonian and diffusive relaxation factors. The choice of the profiles and the values of the coefficients $N(x)$ and $D(x)$ in the relaxation zones control the reflections at the boundary.

The relaxation is implemented after each acoustic step as an implicit correction. We allow $\tilde{\psi}''^{,n+1}$ to denote the perturbation of the updated variable after each acoustic time step. The relaxation is then applied as a correction in a subsequent step using the following implicit flow relaxation equation:

$$\frac{\psi_i''^{,n+1} - \tilde{\psi}_i''^{,n+1}}{\delta\tau} = -N_i\left(\psi_i''^{,n+1} + \psi_i^t - \psi_i^{c,n+1}\right)$$
$$+ \frac{D_i}{\delta x^2}\left\{\left(\psi_{i+1}''^{,n+1} + \psi_{i+1}^t - \psi_{i+1}^{c,n+1}\right)\right.$$
$$- 2\left(\psi_i''^{,n+1} + \psi_i^t - \psi_i^{c,n+1}\right)$$
$$\left. + \left(\psi_{i-1}''^{,n+1} + \psi_{i-1}^t - \psi_{i-1}^{c,n+1}\right)\right\}$$

where $\delta\tau$ is the acoustic time step, δx is the grid spacing and $\psi_i^{c,n+1}$ is the coarse grid value that is interpolated in space and to the time step $(n+1)$. $\psi_i''^{,n+1} = \psi_i^{n+1} - \psi_i^t$, where ψ_i^{n+1} is the total fine grid value, ψ_i^t is the most updated value in the RK step and $\psi_i''^{,n+1}$ is the perturbation, with respect to ψ_i^t. For the prognostic variables, located at half-grid points that are adjacent to the lateral boundary, this implicit equation is solved for $\psi_i''^{,n+1}$ along the relaxation zone, subject to the boundary conditions:

$$\psi_{S+1}''^{,n+1} = \tilde{\psi}_{S+1}''^{,n+1} \text{ and } \psi_1''^{,n+1} = \psi_1^{c,n+1} - \psi_1^t$$

where s is the index of the last relaxed point in the interior of the domain. For the normal velocities at the boundary, the same system will be solved, except that consistency between the coarser and the finer mass fluxes in the continuity equation will be imposed; that is:

$$\nabla \cdot \vec{V} = \nabla \cdot \vec{V}^c$$

where $\vec{V}$ and $\vec{V}^c$ are the velocity vectors from the nested and the coarse grids. Since the tangential velocities that are adjacent to the boundary are imposed by the coarse grid model, the above relation reduces to:

$$\frac{\partial U}{\partial x} = \frac{\partial U^c}{\partial x}$$

where U and U^c are the normal components of $\vec{V}$ and $\vec{V}^c$, respectively. This relationship is imposed implicitly at the lateral boundaries, and the implicit equation is solved for $U''^{,n+1}$ along the relaxation zone as stated above, but with the
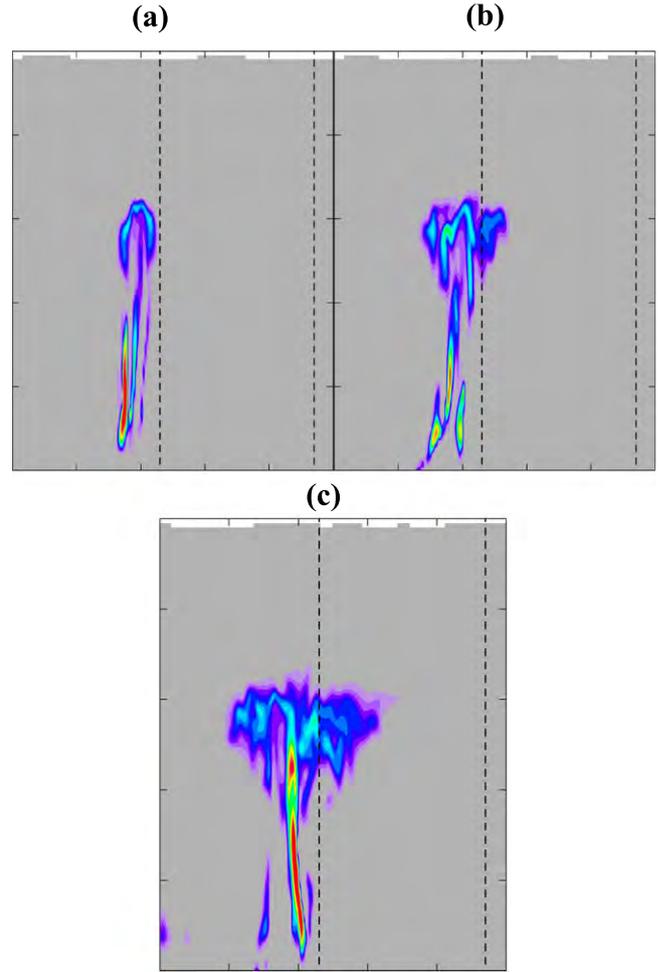

(a)   **(b)**

(c)

Figure 4. Vertical cross sections of density irregularities (color) from large domain simulations at three different times: (a) t1 = 191, (b) t2 = 291 and (c) t3 = 491. The two vertical dashed lines enclose the domain that is used for limited-area simulations.

following implicit boundary conditions:

$$U''^{,n+1}_{s+1} = \tilde{U}''^{,n+1}_{s+1}$$

and

$$U_2''^{,n+1} - U_1''^{,n+1} = \left(U_1^t - U_1^{c,n+1}\right) - \left(U_2^t - U_2^{c,n+1}\right).$$

The Newtonian and diffusive relaxation times are fixed by the choice of the coefficients N_i and D_i. Optimal profiles for the Newtonian relaxation coefficient N are proposed in [10] and [55]. They are constructed in such a way that, under idealized conditions, the unwanted partial reflection of the outgoing waves that leave the domain is minimized. More recently [71], conducted a detailed theoretical and numerical study on the choice of the Newtonian and diffusive relaxation coefficients, in which they compared different profiles and relaxation times. They concluded that a diffusive relaxation, combined with exponential or optimized profiles, gives better results. Also, they presented a formula for what they called the leading coefficients N_2^* and D_2^*, which they derived using the criterion of minimum reflection. These are nondimensional coefficients at the first relaxed grid point. These coefficients,

together with the relaxation profiles, determine the entire relaxation time in the relaxation zone through the relations:

$$N_i = -\frac{c}{2\Delta x}N_2^* \tilde{N}_i \text{ and } D_i = -\frac{c}{2\Delta x}D_2^* \tilde{D}_i$$

In these relations, c is the phase speed of the fastest wave and $\tilde{N}_i$ and $\tilde{D}_i$ are the normalized profiles of the coefficient ($\tilde{N}_1 = 1$ and $\tilde{D}_1 = 1$). In our implicit relaxation, we choose a five-point or nine-point deep relaxation zone, in which the Newtonian and diffusive relaxation times are applied. Following [71], we choose $N_2^* = 0.9$ and $D_2^* = 0.9$; c is the speed of sound, and an optimized profile is computed for $\tilde{N}_i$ and $\tilde{D}_i$ using the algorithm presented in [55]. These specifications entirely determine the Newtonian and diffusive relaxation times.

Figure 4 shows a test of the implicit relaxation for an idealized simulation. It shows cross-sections of density irregularities from a large domain simulation, using open boundary conditions. The grid spacing is 1.5 km. The cross-sections are shown for three different times t1 = 191, t2 = 291 and t3 = 491, after density irregularities have developed. The two vertical dashed lines enclose the nested domain, which is used for limited-area simulations. The nested domain is chosen to be outside the main density anomaly region. This simulation uses a grid spacing that is three times finer than the one used for the large domain simulation. All the fields, including the densities, are relaxed to equal the fields from the large domain by using 5-point-wide implicit relaxation. These tests show that the density irregularity and the associated dynamics smoothly cross the boundary without noticeable reflections. The Newtonian and diffusive relaxation schemes used in the implicit scheme are fixed by the choice of the optimal coefficients that are constructed in such a way that the unwanted partial reflections of the outgoing waves that leave the domain is minimized.

We also mention resolving techniques for front tracking and density current fronts that have been used in the context of neutral fluids in order to study classical Rayleigh–Taylor instabilities ([25]) and the dynamics of fronts of density currents that are associated with geophysical flows ([35, 67]). These efficient computational methods, previously used for neutral fluids, are extended to charged interfaces/fronts in the context of ionospheric dynamics.

3. Multiscale nested simulations of primary and secondary Rayleigh–Taylor instabilities in ionospheric flows, equatorial spread F (ESF)

Plasma irregularities and inhomogeneities in the F region, caused by plasma instabilities, manifest as spread F echoes. The scale sizes of the density irregularities range from a few meters to a few hundred kilometers, and the irregularities can appear at all latitudes. However, spread F echoes in the equatorial region can be particularly severe. At night, fully developed spread F is characterized by plasma bubbles, which are vertically elongated wedges of depleted plasma that drift upward from beneath the bottomside F layer. Under certain

conditions, a density perturbation can trigger the Rayleigh–Taylor instability on the bottomside of the F layer. Once triggered, density irregularites develop, and the field-aligned depletions then bubble up through the F layer. The east-west extent of a disturbed region can extend up to several thousand kilometers, with the horizontal distance between the separate depleted regions extending to tens to hundreds of kilometers. The plasma density in the bubbles can be up to two orders of magnitude lower than that in the surrounding medium. When spread F ends, the upward drift ceases and the bubbles become fossilized.

The evolution of the ESF is a strongly nonlinear phenomenon, with multiscale interactions for ionospheric dynamics. The large-scale primary Rayleigh–Taylor mode can promote a hierarchy of smaller-scale plasma instability processes that give rise to a wide spectrum of irregularities. The presence of these small scale irregularities was evidenced from the observations that showed the coexistence of kilometer disturbances and meter scale disturbances in the nighttime equatorial F region ([7]). Thus, simulations that use coarse and fixed resolutions cannot resolve the small scale disturbances. Poor resolution of these scales can, in turn, affect the accuracy of the larger scales due to nonlinearity. Obviously, one can design a computer model with a very high spatial resolution everywhere. But then, the simulations will be prohibitively expensive, particularly in three dimensions.

Considerable efforts have been made in the development of computer models that simulate the generation and evolution of Equatorial Spread F (ESF) dynamics. Most of these models use periodic boundary conditions with fixed spatial resolutions in both the horizontal and the vertical directions. The transport algorithm that is commonly used in these models is the flux-corrected transport method ([120]). This scheme, however, tends to develop relatively high numerical diffusivity that can be comparable to the physical diffusivity produced by the subgrid scale turbulent mixing [27]. The Crank-Nicholson (C-N) scheme was also used in some ionospheric models ([4, 32]). The C-N scheme, however, can produce excessive noise, thereby degrading the numerical solution.

In this section, nested numerical simulations of ionospheric plasma density structures that are associated with the nonlinear evolution of the Rayleigh–Taylor (RT) instability in the Equatorial Spread F (ESF) are presented. The numerical implementation of the nested model uses a spatial discretization with a C grid staggering configuration, in which normal velocities of ions and electrons are staggered one-half grid length from the density of the charged particles (figures 1 and 2). The advection of charged particles is computed with a fifth-order, accurate in space, Weighted Essentially Non-Oscillatory (WENO) scheme. The continuity equation is integrated using a third-order Runge-Kutta (RK) time integration scheme. The equation for the electric potential is solved at each time step with a multigrid method. For the limited-area and nested simulations, the lateral boundary conditions are treated via implicit relaxation, which is applied in the buffer zones where the density of the charged particles for each nest is relaxed to the density of the charged particles obtained from the parent domain (figure 3). High resolution in targeted regions,

offered by the nested model, is able to resolve secondary RT instabilities and to improve the resolution of the primary RT bubble compared to the coarser large domain model. The computational results are validated via a large domain simulation, in which the resolution is increased everywhere.

The equatorial ionosphere is considered in a slab geometry, with Earth's magnetic field **B** directed along the y axis. We choose the unit vectors $\mathbf{i}$, $\mathbf{j} = \mathbf{B}/B$ and $\mathbf{k}$ to be directed

along the westward, northward and upward directions, respectively. A set of plasma two fluid equations, which describe the conservation of momentum, mass and current, are considered. These equations govern the motion of the species s ions ($s = i$) and the electrons ($s = e$), the masses of which are represented as Mi and Me, respectively. The computational methodology that is presented in section 2 is validated via a large domain simulation of the interaction of
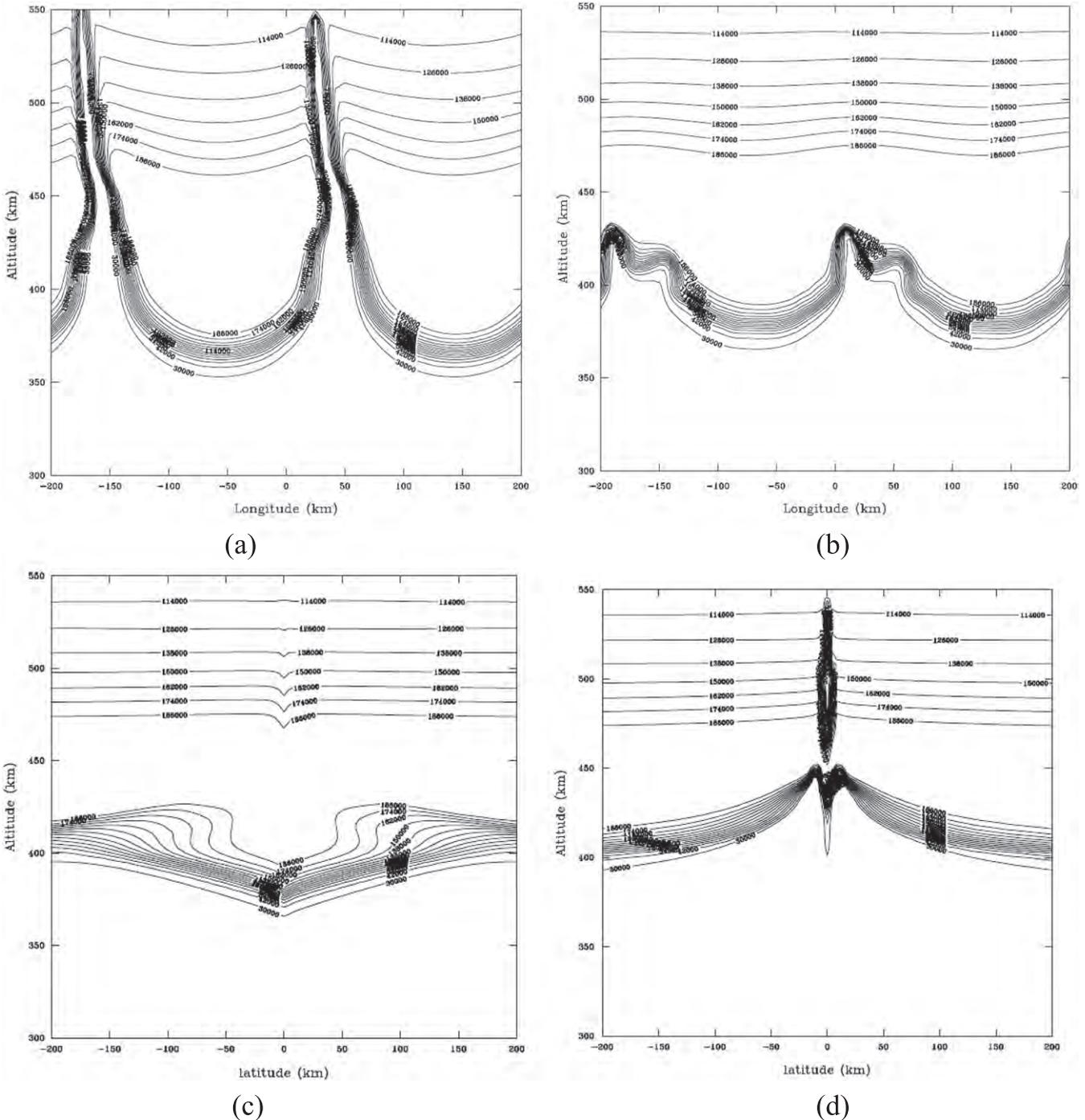

(a)

(b)

(c)

(d)

Figure 5. 3D large domain simulation of the ESF. The neutral wind is 125 m s^{-1}, and the imposed external electric field is given by $E_{\mathrm{o}}/B = 100$, where B is the magnetic field. The horizontal axis represents the east–west range (a) and (b), and the north–south range (c) and (d). The solid curves represent the iso-density contours after 2000 s. The simulation is initialized with a small 3D density perturbation that is superimposed with the background density profile. The x–z cross-sections are at (a) $y = 0$ km and (b) $y = 109$ km. The y–z cross-sections are at (c) at $x = 0$ and (d) $x = 31$ km.

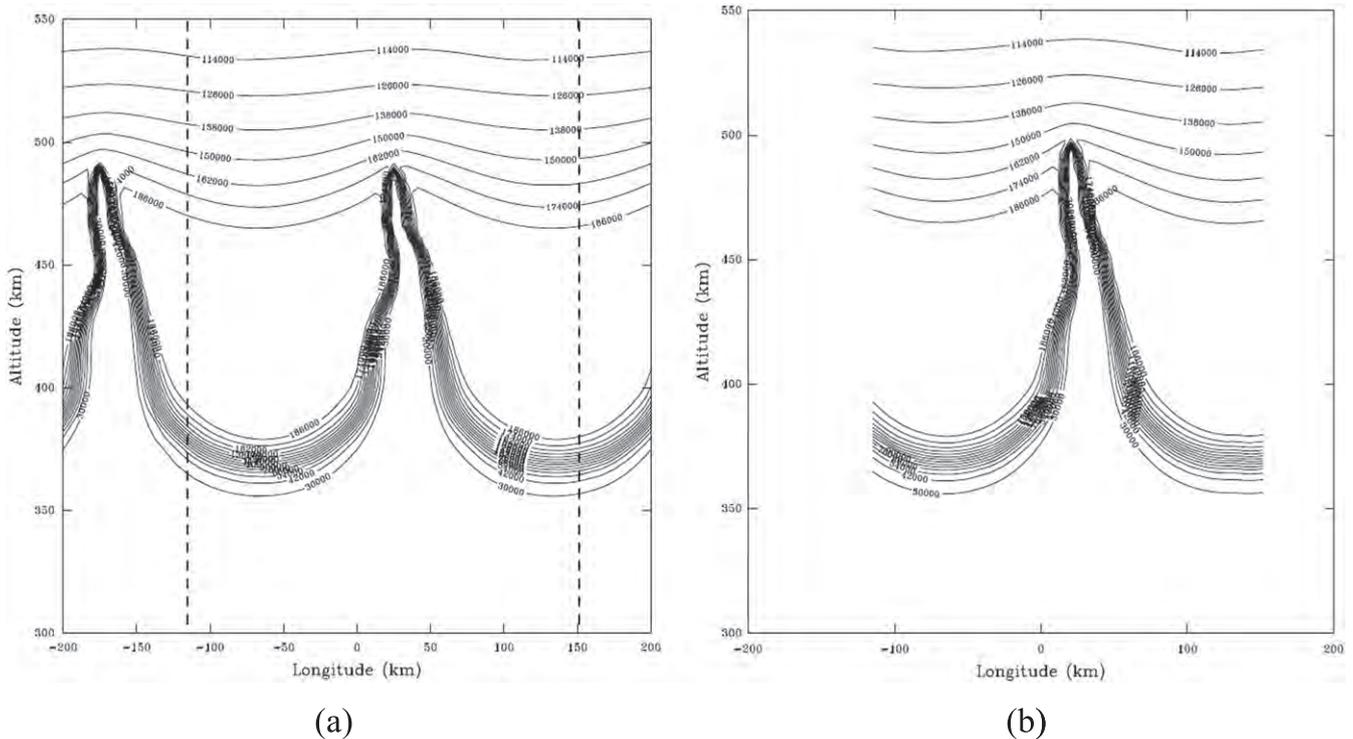(a)   (b)

Figure 6. (a) Large domain simulation of the ESF. The neutral wind magnitude is 125 m s^{-1}, and the imposed external electric field is given by $E_o/B = 100$, where B is the magnetic field. The horizontal axis represents the east–west range. The cross-section is taken at y = 0. The solid curves represents the iso-density contours after 2000 s. The simulation is initialized with a small density perturbation that is superimposed on the background density profile. The two dashed vertical lines represent the horizontal boundary of the domain used in the limited area and the nested simulations. (b) Limited area domain simulation of the ESF. The lateral boundary conditions use the implicit relaxation that is applied in buffer zones where the density of the charged particles is relaxed to equal the density of the charged particles obtained from the parent domain, shown in (a). The horizontal axis represents the east–west range. The solid curves represent the iso-density contours after 2000 s. The simulation is initialized with a small density perturbation that is superimposed with the background density profile. The horizontal grid spacing is the same as the spacing in the simulation shown in (a).

the equatorial ionosphere with the eastward F region neutral wind in the presence of evolving spread F bubbles. Standard background profiles of ion-neutral collision frequency, recombination and the background electron density profile as a function of altitude are used in the numerical simulations ([58, 99, 100]). An assessment of the performance of local ensemble Kalman filter data assimilation techniques applied to the ionospheric flows is given in [16].

The extent of the large domain simulation is [−200 km, 200 km] in the horizontal direction and [300 km, 550 km] in the vertical direction, with a grid spacing of 4 km, and 2.5 km in horizontal directions and vertical directions, respectively. Figure 5 shows a 3D large domain simulation of the Equatorial Spread F (ESF). The neutral wind is 125 m s^{-1}, and the imposed external electric field is given by Eo/B = 100, where B is the magnetic field. The horizontal axis represents the east-west range, (a) and (b), and the north-south range, (c) and (d). The solid curves represent the iso-density contours after 2000 s. The simulation is initialized with a small 3D density perturbation superimposed to the background density profile. The x-z cross-sections are at (a) y = 0 km and (b) y = 109 km. The y-z cross-sections are at (c) at x = 0 and (d) x = 31 km. The development of the ESF as a large-scale bubble is evident. The top of this bubble reaches a high altitude and is located below 500 km. We note that our model does not

develop spurious small-scale numerical noise, which occurred in the Crank-Nicholson scheme in [5].

To test the performance of the lateral implicit relaxation, the outputs from the large domain are truncated within a limited area [−125 km, 150 km], which is represented by the dashed vertical lines in figure 6; and a second simulation is conducted using the same model within this limited area without increasing the resolution (with 4 km horizontal grid spacing). This simulation uses the same configuration that was used in the large domain (same horizontal and vertical grid distributions), except that the number of grid points in the horizontal is reduced; and both the electric potential and plasma density are specified at the lateral boundaries. The density computed from the nested model is relaxed to the coarse outputs from the large domain by using the implicit relaxation. The width of the relaxation zone is five points. Figure 6 shows the field of the iso-density contours, simulated by the limited-area model after 2000 s. The simulation results from the large domain (figure 5) and from the limited-area domain (figure 6) are indistinguishable over the limited-area domain, thereby demonstrating that the nested model and the method proposed for the relaxation perform well.

To test the impact of the resolution on the evolution of the ESF, a nested simulation was conducted using the same setup as the one used for the limited area simulation, but the
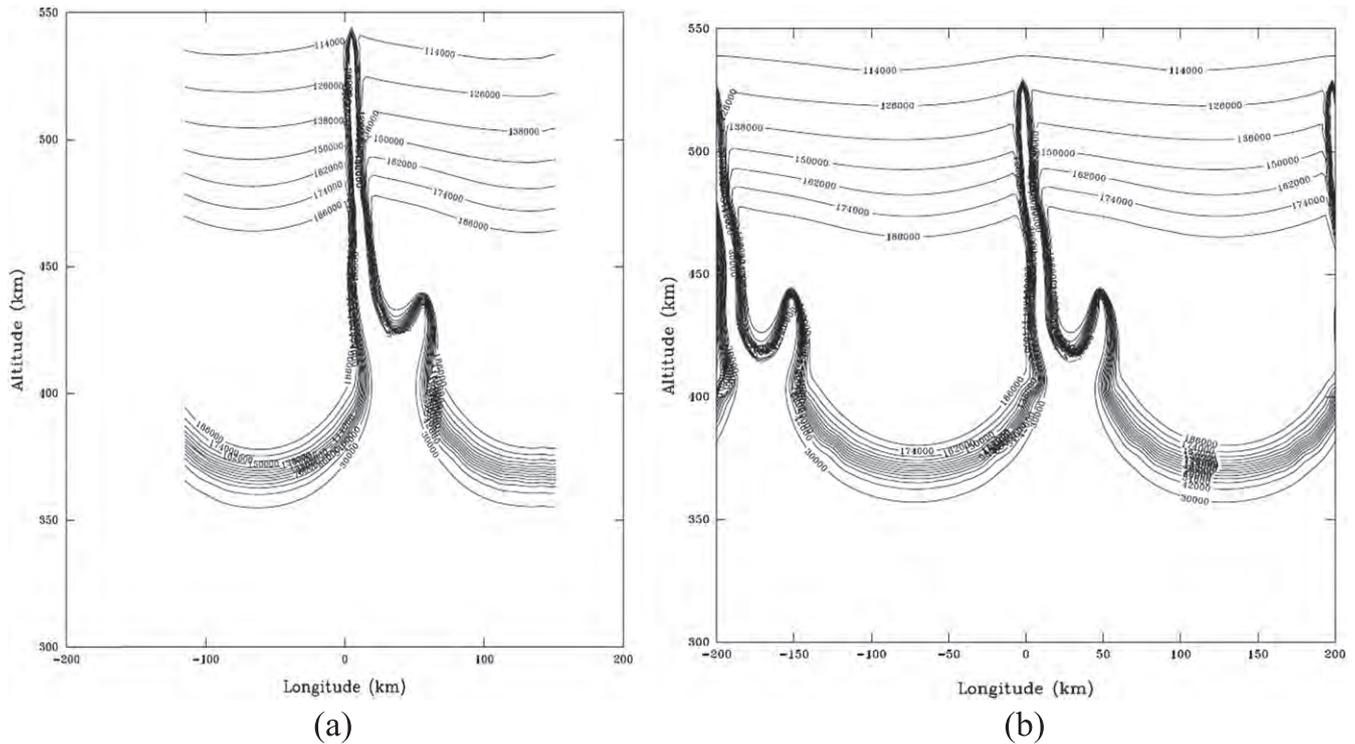
(a)   (b)

Figure 7. (a) Nested domain simulation of ESF. The resolution is doubled (in the finest nest only). The lateral boundary conditions use the implicit relaxation that is applied in the buffer zones where the density of the charged particles is relaxed to equal the density of the charged particles interpolated from the parent domain. The solid curves represent the iso-density contours after 2000 s. The simulation is initialized with a small density perturbation that is superimposed on the background density profile. Note that the nested simulation resolves the secondary RT instabilities. Also, the primary disturbance is more developed and reaches higher altitudes. (b) Large domain simulation with high resolution (the resolution is doubled everywhere). This demonstrates that the secondary RT instabilities (bubbles) that are resolved by the nested simulations are not artifacts, and that the nesting offers more accurate results at low computational cost.

resolution is doubled (the horizontal grid spacing is 2 km). The lateral boundary conditions use the implicit relaxation that is applied in the buffer zones where the density of the charged particles of the nest is relaxed to equal the density of the charged particles of the nest that are interpolated in time and space from the parent domain, as described in section 2. Figure 7 shows the field of iso-density contours, simulated by the nested model after 2000 s. The results show that in addition to the main spread F bubble that was also resolved in the large domain simulation, there is a generation of secondary Rayleigh–Taylor instabilities or secondary bubbles that were not resolved in the coarse grid simulation. In addition, the primary (the large scale) disturbance is more developed and reaches higher altitudes.

To show that the secondary ESF instability and the higher altitude of the top of the main bubble are not artifacts due to numerical errors in the nested model, another simulation was conducted.

We used a large domain, as was also used in the first simulation; however, in the second simulation, the resolution was doubled everywhere. The results of this simulation are presented in figure 8. We noted that by increasing the resolution of the parent model, the secondary instability was now resolved, as in the nested simulation (figure 7). Also, the primary disturbance is more developed and reaches a higher altitude (above 500 km) as the resolution is doubled. Thus, the high resolution in the targeted

regions offered by the nested model is found to be critical for the resolution of the small-scale ionospheric plasma density structures and for the improvement of the large-scale bubble, which are associated with the evolution of the primary and secondary Rayleigh–Taylor instabilities in the Equatorial Spread F.

4. Impacts of time varying neutral winds on fine scale structure of sporadic E and intermediate layers

In this section, we present three-dimensional numerical studies of the E and lower F region ionosphere, coupled with the neutral atmosphere dynamics. The inclusion of neutral dynamics in the model allows us to study the transport patterns of plasma density and to examine the charge of the neutral interactions over the full evolution cycle of an inertial gravity wave when the background flow spins up from rest, saturates and eventually breaks. Using Lagrangian analyses, we show the mixing patterns of the ionospheric responses, formation and subsequent evolution of nonequilibrium ionospheric layers. The corresponding plasma density in this flow develops complex wave structures and small-scale patches during the gravity wave breaking event.

The lower ionospheric altitudes are challenging to model because they are too low for orbiters and too high for
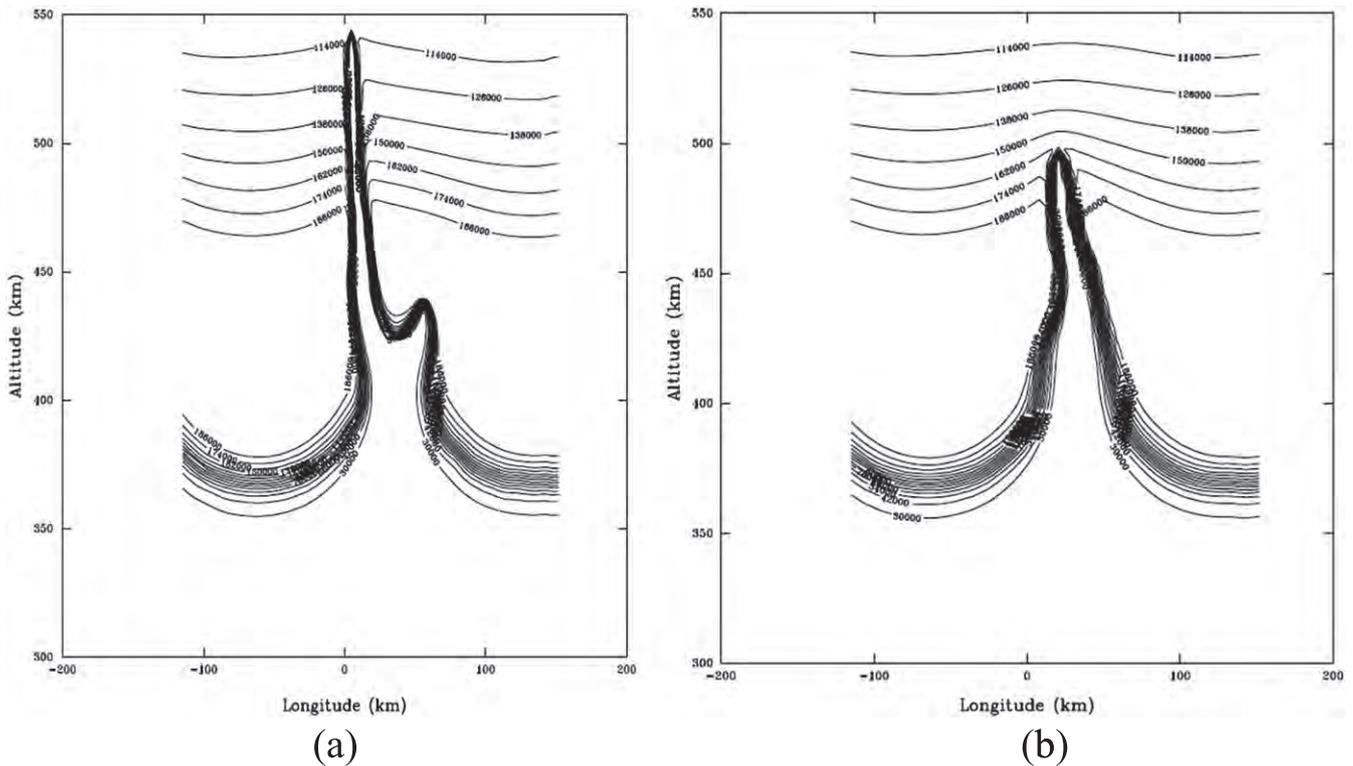
Figure 8. Nesting summary: high resolution modeling of the multiscale ionospheric dynamics over a limited spatial range in the altitude, latitude and longitude, which provides accurate results at a low computational cost. (a) With nesting and implicit relaxation to the coarse model (results verified by high resolution computations on a large domain) and (b) without nesting.

radiosondes to take direct measurements. In recent years, computer simulations of the Earth's ionosphere have become a prevailing tool used to obtain properties of plasma flows in the ionosphere, especially at low altitudes. Numerical models have been developed to study Rayleigh–Taylor instabilities in the equatorial spread F and ionospheric responses to neutral atmospheric motions in mid-latitude. In these studies, the neutral dynamics are prescribed as idealized velocity fields, such as a constant drift flow or empirical shear flow models; and they are specifically used for mid-latitude simulations, linear models of inertial gravity waves (IGW) or data sets from other atmospheric models, which are influenced by many dynamical processes.

We study 3D dynamics in the E- and F-region of the ionosphere due to interactions with neutral winds. A parallelized DNS solver is used to solve the coupled system of charged flows and the 3D Navier–Stokes equations for neutrals. In the current literature, the background neutral flow is usually prescribed and not coupled into the dynamics. We include this coupling permitting time-dependent neutral winds in the model ([58, 99, 100]). Multi-nested limited-area high resolution simulations of the ionosphere for a range of altitudes from 80 km to 500 km, which resolve the coupling between time-dependent neutral winds and ions/electrons at mesoscale/microscale resolutions, are conducted.

Sharply defined layers/density interfaces determine fine scale structure of the ionosphere. Charged shear layers form along contours that are defined by very large gradients in densities and scintillations. Inhomogeneous turbulent

dynamics, which are adjacent to these layers, stretch and distort the larger scales in order to counter the tendency of the interface to thicken. Our focus is on the multiscale dynamics of the flow within and near the density interfaces (electron density/ionization fronts). The root mean square values of density and velocity, and also their flatness factors, are given by statistical averaging across these layers, taking into account the degree to which the thin layers are sufficiently convoluted to be 'space-filling', with the thickness of the layer edges being approximately equal to the Taylor microscale. Through the blocking of the external scale eddies, which occur outside the layers as they impinge onto the interfaces, upscale and downscale energy transfer processes lead to distorted inertial-range motions with a wide range of length scales and characteristic self-similar power-law spectra. Here, the skewness of the velocity derivatives becomes negative. The local dynamics near such density interfaces (inhomogeneous, non-Kolmogorov) is quite different to dynamics in which a wide spectrum of eddies interact homogeneously through the flow (homogeneous, isotropic Kolmogorov turbulence). The structure of these thin layers is identified by conditionally averaging the fields relative to the moving interface. The shear layer itself is unstable and generates eddies on the scale of the shear layer thickness. These strongly influence the average movement of the interface. Simulations show how the interface moves outward at the boundary entrainment velocity. The very high velocity gradients across the thin layer are maintained by the interaction between the large-scale impinging eddies and the large-scale

shear outside the interface. Note that conventional turbulence models, even when used for unsteady flows, simulate the energetic diffusive action of small-scale eddies and not the counter-diffusion action of highly inhomogeneous larger-scale eddies near the interfaces. Even if the initial third moments (or skewness) of the large and small scale gradients are zero, these interactions generate a negative third moment of the derivatives. The mechanism also leads to the third moment of the velocity fluctuations being negative as a result. The very high velocity gradients that separate regions of flows with differing levels of densities have a complex geometry.

Polarization charges tend to accumulate at sharply defined density interfaces ([99, 100]). As many researchers have commented, new concepts are needed in order to understand the spatially intermittent structure of turbulent interfaces. As for other well-defined large-scale coherent structures, a combination of quasi-deterministic modeling of the defined types of the interface structure and the probabilistic analysis of their occurrence can describe the characteristic features as well as their overall statistics. This approach can overcome substantial disadvantages of the current statistical modeling approach by providing physical explanations of the key features of charged turbulent interfaces, namely, the extreme non-Gaussianity of its smallest scales and its critical upscale transfer processes, which lead to the formation of internal shear layers. High resolution simulations, with combined Eulerian and Lagrangian techniques, allow us to resolve the sharpness of the charged density interfaces, which are often overlooked.

The fine scale structure of the 3D time-mean electron/ion density distributions are determined by time-mean vertical and horizontal electron/ion density fluxes: $\langle \rho_e' w' \rangle$, $\langle \rho_e' u' \rangle$, $\langle \rho_e' v' \rangle$. Here, electron/ion densities and velocities are decomposed into ensemble means and fluctuations $\rho = \langle \rho \rangle + \langle \rho_e' \rangle$, $u = \langle u \rangle + u'$, $v = \langle v \rangle + v'$, $w = \langle w \rangle + w'$. The effects of ionospheric processes on the variance of spatial density anomalies at ionospheric meso/micro scales need to be assessed. If a process generates spatial density anomalies, whether they are positive or negative, it leads to an increase in $(\rho_e')^2$. There are several processes capable of affecting the electron/ion density fields. One is related to electron/ion vertical motions. Here, the question of primary interest is the sign of the term $\langle \rho_e' w' \rangle$, normalized by variances of ρ_e' and w'. Another process capable of affecting the 3D density distribution is related to density fluxes, which are induced by eddies that are associated with neutral velocities. The term $\langle \rho_e' w' \rangle$ represents the generation of spatial electron/ion density anomalies through vertical motions; $(\rho_e')^2$ are generated by upward motions in regions with higher electron/ion densities or by downward motions in regions with lower densities. Similarly, the terms $\langle \rho_e' u' \rangle$ and $\langle \rho_e' v' \rangle$ are responsible for horizontal fluxes and are of particular interest in assessing the relative importance of various processes used in the generation and the destruction of spatial electron/ion density anomalies. We investigate the generation and the destruction of spatial density anomalies through the ensemble and time-mean fluxes associated with the mean vertical and horizontal motions and through the density fluxes induced by time dependent velocities.

We note that vertical motions can alter the electron density distribution at ionospheric meso/microscales. We compare the distribution of $\langle w' \rangle$ with that of $\langle \rho_e' \rangle$ to identify altitudes in which the lower electron density regions sink and altitudes in which the higher electron density regions rise. These vertical motions lead to a generation of spatial electron density anomalies. When integrated over the area of the density layer, a net generation of spatial density anomalies through time-mean vertical motions can be found. The vertical profile of $\langle \rho_e' w' \rangle$, integrated over each density layer, is of particular interest. We identify altitudes where large contributions come from the vertical density flux. Similar to vertical motions, horizontal density fluxes $\langle \rho_e' u' \rangle$ and $\langle \rho_e' v' \rangle$, which are induced by u' and v', can affect the electron/ion density fields in the mesoscale/microscale domain. Detailed temporal and spatial characteristics of fluctuating density interfaces (electron density and ionization fronts) were investigated in [58, 99, 100].

Sporadic E layers are ionization enhancements in the E region at altitudes between 90 and 120 km. The layers tend to occur intermittently and can be seen at all latitudes. Sporadic E layers at mid-latitudes are primarily a result of wind shears ([88]), but they can also be created by diurnal and semi-diurnal tides. The layers are formed when the vertical ion drift changes direction with the altitude, and the layers occur at the altitudes where the ion drift converges. In the E region, the zonal neutral wind is primarily responsible for inducing vertical ion drifts, which result from a dynamo action. A reversal of the zonal neutral wind with the altitude results in ion convergence and divergence regions. The helical nonparallel neutral flows are frequently observed in the lower ionosphere at mid-latitudes. Three-dimensional shear instabilities, which are attributed to the breakdown of polarized wind fields, are common at ionospheric altitudes that encompass the E layers. These flows are characterized by neutral wind profiles with intense variations in both eastward and westward components over a short vertical distance. This intense nonparallel shear can lead to the development of 3D helical Kelvin-Helmholtz instability, with characteristics that are different from the one found in the parallel flows. The stability criterion for a general nonparallel polarized wind field has been recently established in [56]. Contrary to the parallel flows, this criterion is anisotropic and depends on the direction of the wave vectors of the unstable modes. The physical and dynamical processes associated with polarized instabilities are inherently three-dimensional. The horizontal velocity vector $\left(\bar{U}(x_3) \right.$ and $\left. \bar{V}(x_3) \right)$ (horizontally and time averaged) rotates with the vertical coordinate (x_3). We allow $\alpha(x_3)$ to denote the angle between the vector $\frac{d\bar{U}(x_3)}{dx_3} = \left(\frac{d\bar{U}(x_3)}{dx_3}, \frac{d\bar{V}(x_3)}{dx_3} \right)$ and the horizontal wave vector. Then, we can obtain the following expression for the *polarized plasma Richardson number*:

$$Ri_p(x_3) = \frac{N^2(x_3)}{\left(\left(\frac{d\bar{U}(x_3)}{dx_3} \right)^2 + \left(\frac{d\bar{V}(x_3)}{dx_3} \right)^2 \right) \cos^2(\alpha(x_3))},$$

Here, the definition of N is based on the number density n instead of the temperature, $N^2 = \frac{(g \partial n / \partial x_3)}{n}$. The polarized plasma
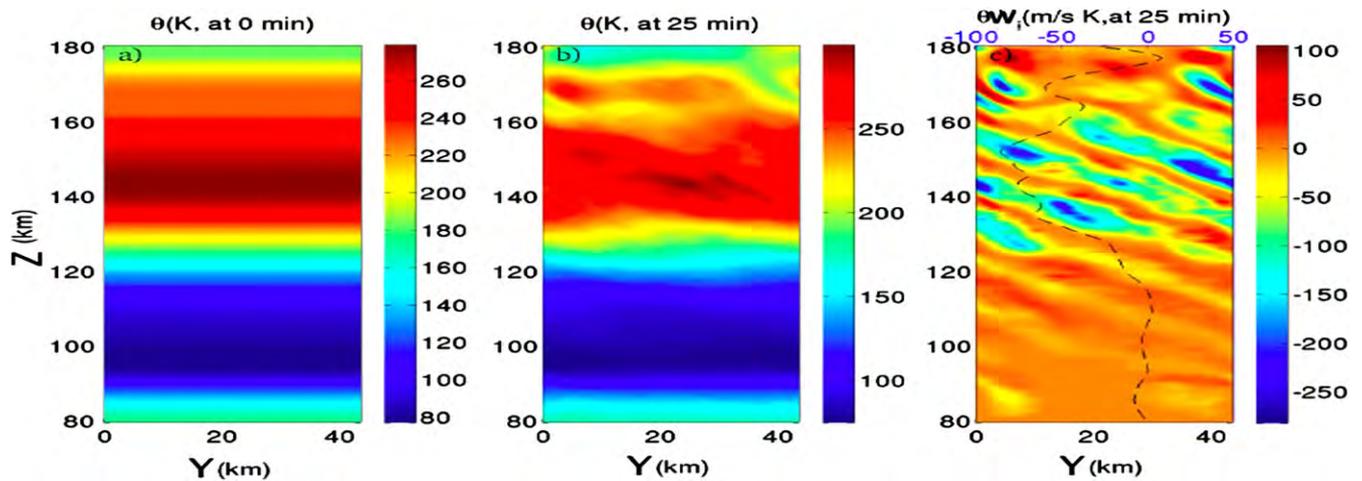
Figure 9. Heat flux shows strong vertical mixing.

Richardson number takes into account horizontal anisotropy, the angle between the horizontal wave vectors and the velocity vectors at each vertical level. In the case of polarized wind fields in stably stratified neutral environments, the polarized Richardson number was rigorously introduced in [56, 66]. The above expression generalizes this definition to ionospheric flows, in which the electron number density is used in place of the temperature, since the ionosphere is stratified with respect to the electron density. Kelley ([50], Page 159) discusses a plasma Richardson number, in the context of parallel flows in the ionosphere, and the role of velocity shear in triggering convective ionospheric storms. The above expression generalizes his definition.

In contrast to sporadic E layers, intermediate layers are broad (10–20 km wide) and occur in the altitude range of 120–180 km. They frequently appear at night in the valley between the E and F regions, but they can also appear during the day. They tend to form on the bottomside of the F region and then slowly descend throughout the night toward the E region. As with sporadic E layers, intermediate layers can occur at all latitudes, have a large horizontal extent, and

In contrast to sporadic E layers, intermediate layers are broad (10–20 km wide) and occur in the altitude range of 120–180 km. They frequently appear at night in the valley between the E and F regions, but they can also appear during the day. They tend to form on the bottomside of the F region and then slowly descend throughout the night toward the E region. As with sporadic E layers, intermediate layers can occur at all latitudes, have a large horizontal extent, and have an order of magnitude density enhancement relative to the background densities ([88]). Intermediate layers are primarily a result of wind shears connected with the semi-diurnal tide. In the E-F region valley (130–180 km), the meridional neutral wind is mainly responsible for inducing the upward and downward ion drifts. When the wind blows toward the poles, a downward ion drift is induced; and when it blows toward the equator, an upward ion drift is induced. If the wind changes direction with the altitude (a helical wind shear), the plasma will either diverge and decrease its density or converge and increase its density (layer formation). When a null

in the wind shear moves down in altitude, the ion convergence region, and hence, the intermediate layer, also descend. Many `active experiments' have been conducted to excite plasma instabilities by creating artificial plasma density gradients and observing the resulting layered structures and their nonequilibrium dynamics. The active technique is to inject large amounts of tracer (barium gas) into the ionosphere from a rocket. The barium is ionized by sunlight and, if released at sunset or sunrise, results in a visible long-lived plasma made usable by the resonant scattering of sunlight. Figure 6.17, from [50], shows visualization of the F-layer plasma instabilities using this Lagrangian tracer technique. The instability triggering plasma turbulence is the generalized Rayleigh–Taylor instability.

Our previous work has focused on the upper troposphere and lower stratosphere (UTLS) shear-stratified dynamics of the neutral atmospheric layers ([51, 56, 59, 60, 62, 63, 65, 66]). Detailed theoretical investigations and high resolution nested calculations were performed to study the variability of the turbulent length scales (Tatarski, Ozmidov, buoyancy, shear) and the fluxes in the UTLS. The upper mesosphere and lower thermosphere region (UMLT internal layer), encompassing 80 km–150 km altitudes, poses similar challenges regarding the characterization of the shear stratified dynamics of the neutral winds. This transformative layer marks the transition to patchy ionospheric turbulence, which is characterized by strong scintillations and anisotropies that are induced by the Earth's magnetic field. Polarized winds throughout the lower thermosphere blow at hurricane speeds of up to $150 \, \mathrm{m \, s^{-1}}$ and produce enormous wind shears. The UMLT layer is a low boundary for the E/F layers, so the information on the variability of the scales and fluxes is needed for computational benchmarks and parameterizations. Most recently, computer simulation models of the Equatorial Spread F (ESF) plumes, or 'bubbles,' have been developed ([31, 41, 58, 83, 84, 99, 100]).

Now, we present three-dimensional numerical results for the E and lower F region ionosphere, coupled with the neutral atmosphere dynamics. The inclusion of neutral time-dependent and turbulent dynamics in the model allows us to
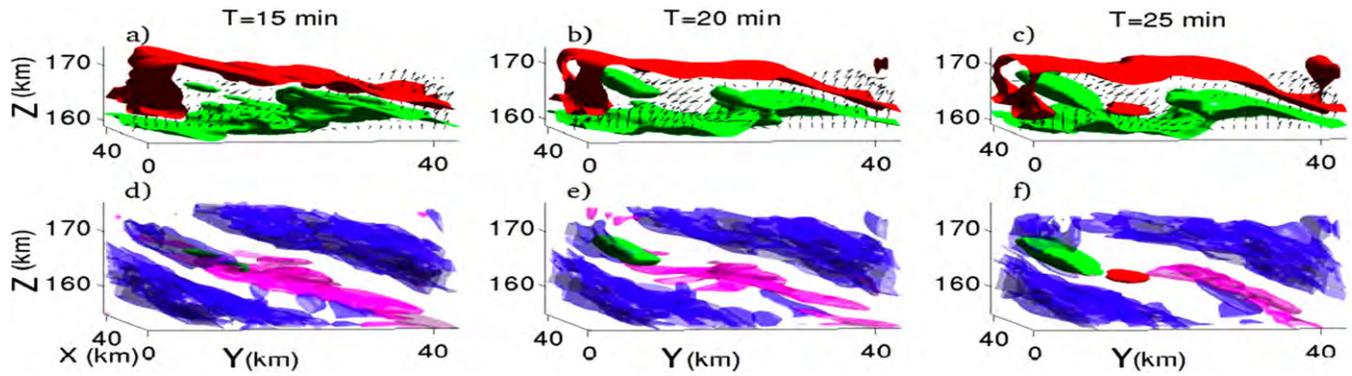
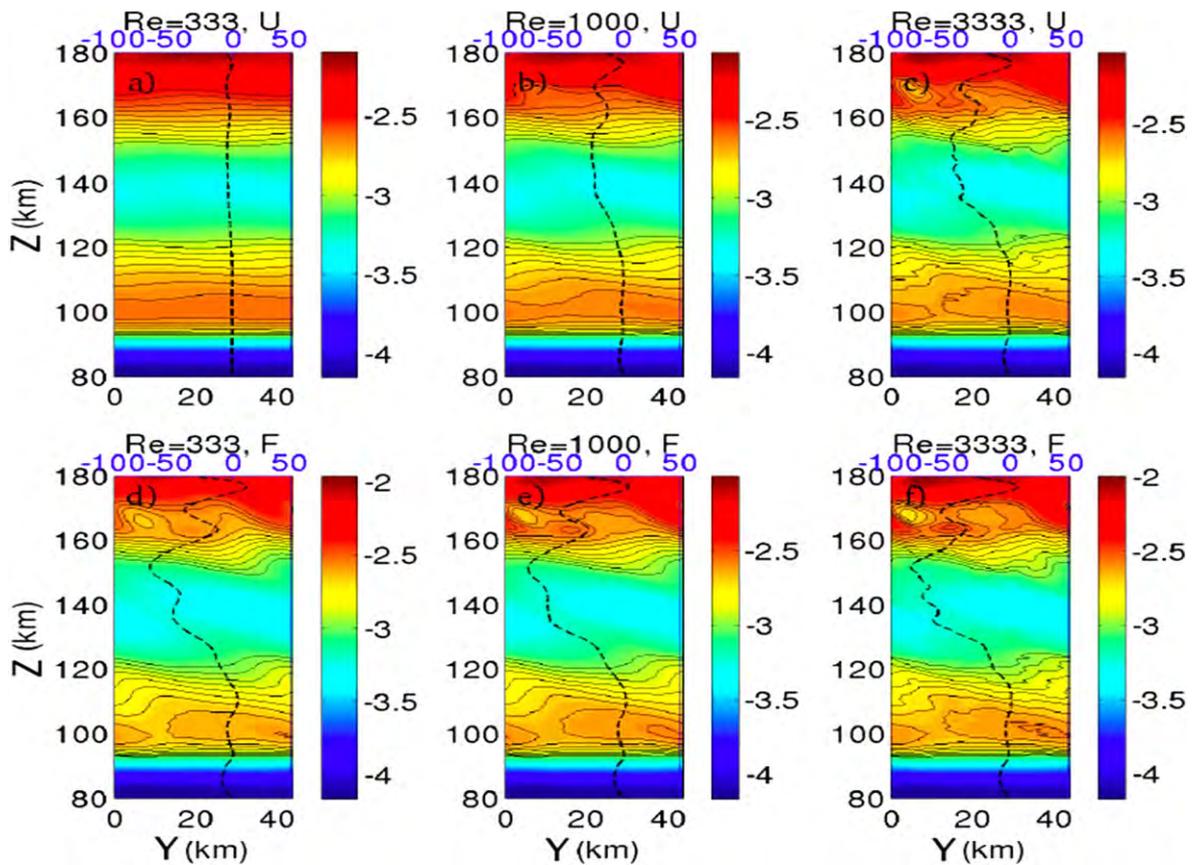**Figure 10.** Evolution of density structures.

Figure 11. Parametric dependence of the emerging density structures and fluxes on the turbulent dynamics of the neutrals.

examine the charge-neutral interactions over the full evolution cycle of an inertial gravity wave when the background flow spins up from rest, saturates and eventually breaks. Using Lagrangian analyses, we show the mixing patterns of the ionospheric responses and the formation of ionospheric layers. The corresponding plasma density in this flow develops complex wave structures and small-scale patches during the gravity wave breaking event. More results can be found in [58, 99, 100].

The heat flux shows strong vertical mixing in figure 9. The evolution of the density structures/interfaces is highlighted in figure 10. The parametric dependence of the emerging density structures and fluxes on the turbulent dynamics of the neutrals is illustrated in figure 11. The plasma density and the electrostatic potential are spun together with the neutral flow from time $T = 0$. We show these two fields in figure 12. The E layer is strongly modified, and the ion density is aligned with the inertia gravity wave phase. Figure 12 shows the plasma response to the wave breaking, including the plasma density structure development. The electrostatic potential becomes strongly field-aligned.

The plasma diffusivity tensor, given in [99], is controlled by the collison frequency, the Boltzmann constant and the plasma temperature. In figure 12, the electrostatic potential shows a strong signature of field alignment throughout the entire simulated column, yet some inertia-gravity wave
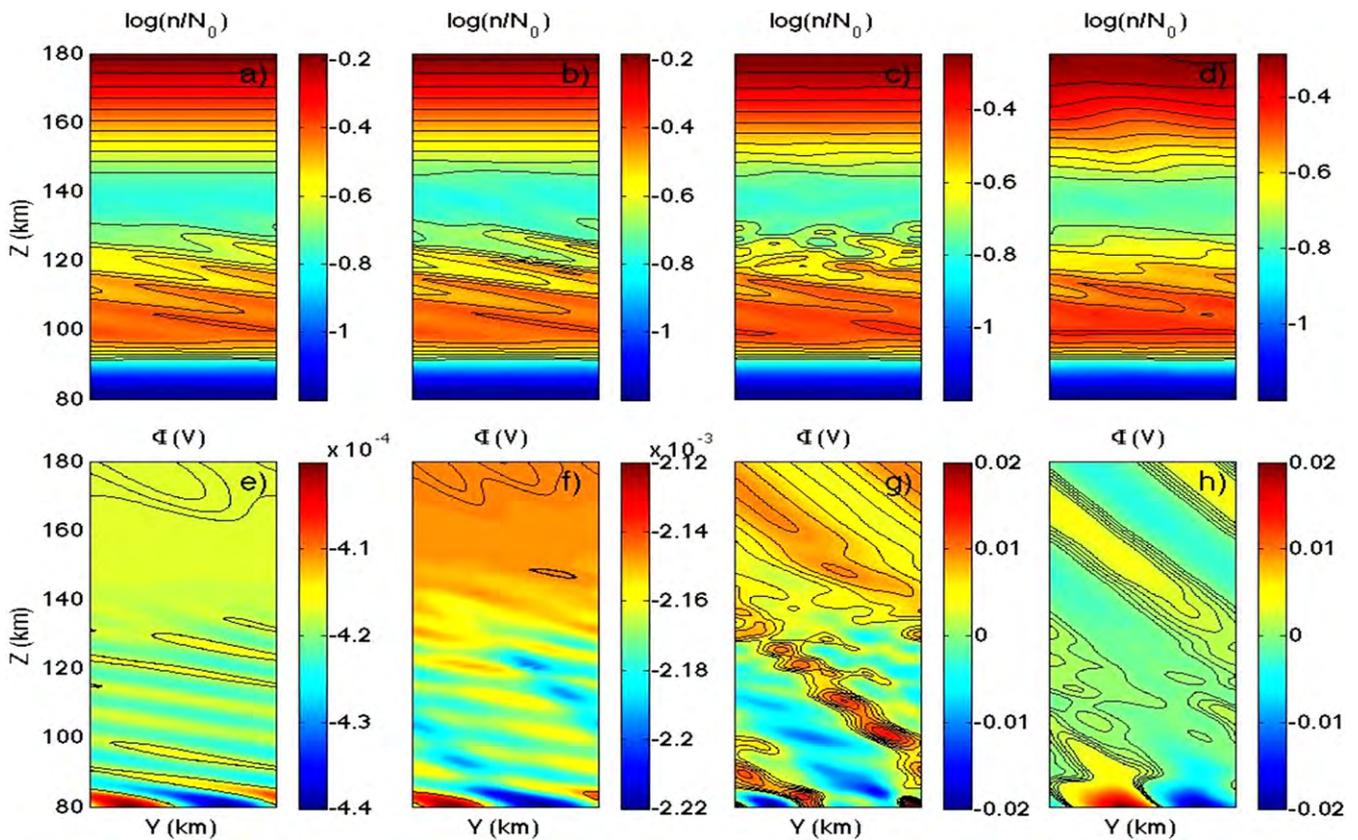
Figure 12. Plasma response to wave breaking and plasma density structure development. The electrostatic potential becomes strongly field-aligned.

structure can still be observed at the bottom of the domain. As the flow develops, the plasma number density becomes strongly undulated. The plasma response to the wave breaking and the complexity of the horizontal structures at wave breaking is shown in figure 13. Panel a) shows the neutral vertical velocity. Panel b) shows the ion vertical velocity. It is predominantly along the wave phase, but has strong three-dimensional perturbations. Note that the velocity structures for the vertical components of the neutral and ion velocities are quite different. Panels c) and d) show the ion density and the electrostatic potential, correspondingly. It is interesting to note that the small-scale perturbations along the wave phase create very strong signals in the electrostatic potential. These signals are also aligned with the magnetic field line.

To better reveal the mixing geometry of the plasma density, we use Lagrangian Coherent Structures (LCS) from the ion velocity to extract the mixing patterns for charged particles ([100]). Before the wave break, the structures are somewhat trivial in that they simply align with the inertia gravity waves (IGW); these structures highlight the shear between the wave phases. After the wave break, the flow is dominant with the small-scale structures, which may lose their coherence during shorter times. As such, we only explore LCS during the wave break event. We focus in the region where the large overturning of the neutral velocity forces the ion disturbance to break up into patches. The closeness in time reveals the evolution of the density patches and

the LCS; hence, this helps to explain the role that LCS plays in organizing plasma density structures. After the flow develops coherent structures, we use the Lagrangian analysis to characterize its topology so as to reveal fine scale structures and mixing patterns for scalar fields, such as the charge density. LCS are made up of distinguished material lines/surfaces that attract/repel local trajectories at the maximal rates. In recent times, the finite-time Lyapunov exponents (FTLE) have conventionally been used to extract the LCS. Based on the local dynamics of the trajectories, the FTLE offers an objective description of how nearby trajectories stretch with the background flow. As a result, local material lines that repel nearby trajectories the most are identified. Reciprocally, attractors are found to be local maximizers of the FTLE when trajectories are integrated in backward-time. Note that large separation of trajectories could also be due to strong shear.

Figure 14 shows the evolution of the plasma density and the LCS for a cross-section. The Lagrangian integration time is chosen to be half of a wave period. Since the structures at this time are predominantly along the streamwise direction, one vertical slice is sufficient to indicate the entire flow structure. In panels a) and d), the plasma density at these two times is shown. It is apparent that plasma density striations break up into small lumps and shed from the main continuous wave phase. In panels b) and e), the forward-time FTLE field, together with the plasma density iso-contour, is shown at
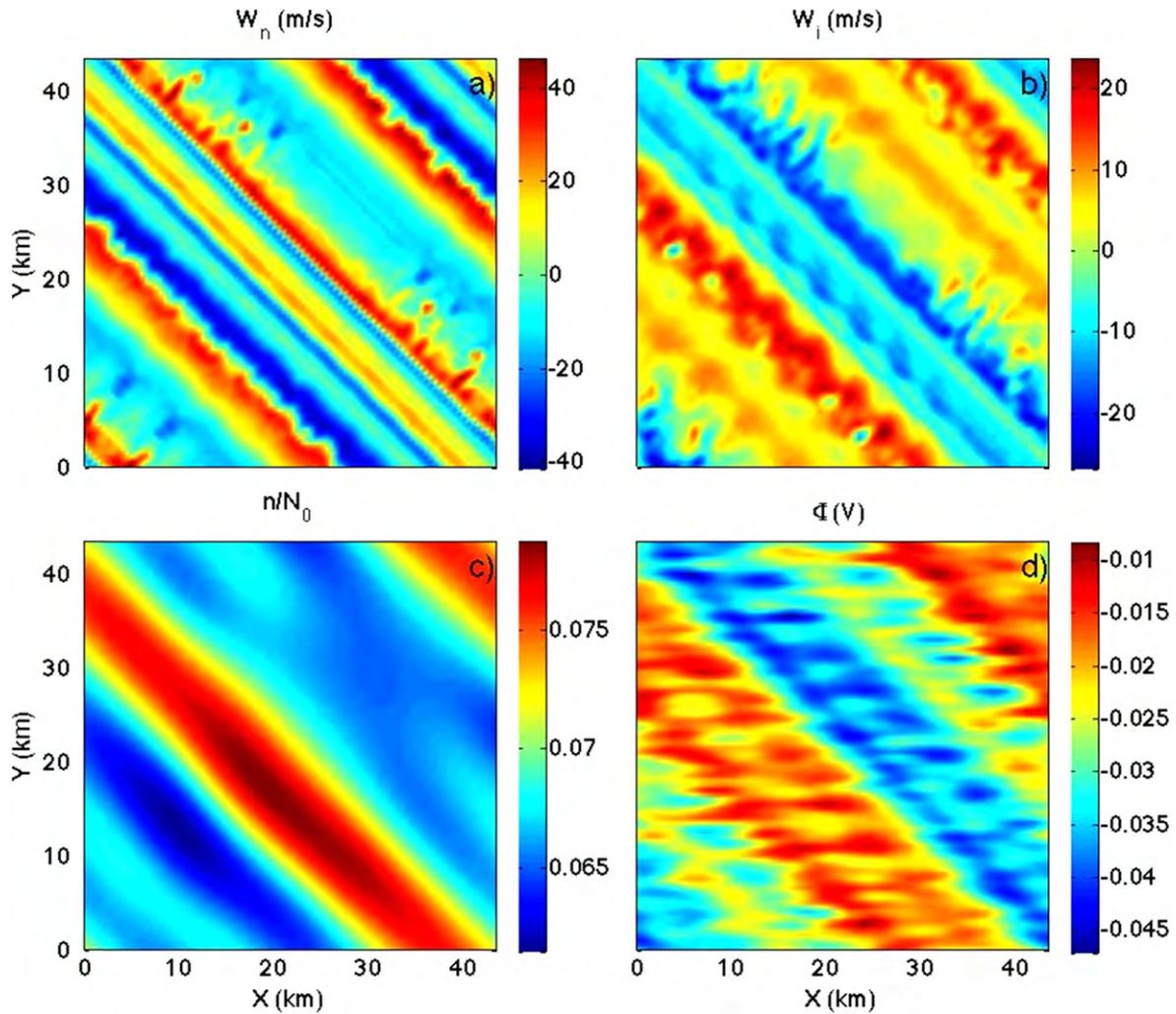
Figure 13. Plasma response to wave breaking: complexity of the horizontal structures at wave breaking.
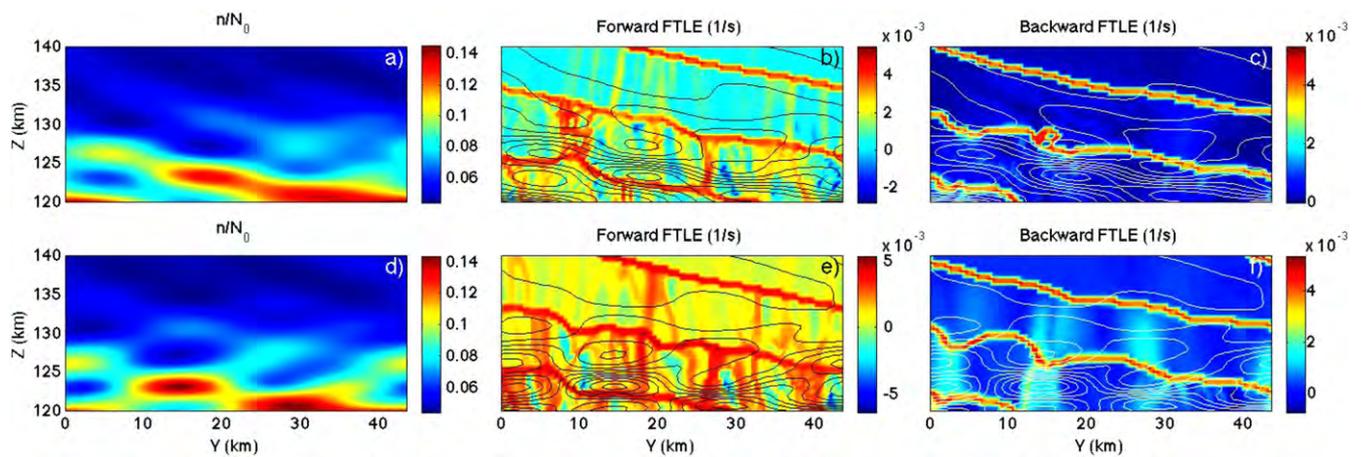

Figure 14. Evolution of plasma density and the Lagrangian coherent structures: (a), (d) plasma density, (b), (e) forward time FTLE, (c), (f) backward-time FTLE. The plasma density contours show a correlation between the LCS and the plasma density (scalar).

these two times. The most dominant feature is the high-lighting red lines along the IGW wave phase. This is not surprising, since the shear in the polarized IGW will create large separation. What is really interesting is the development of the vertical highlighters in both panels. These separating lines divide the wave phase into small compartments, which house one pair of high and low density patches. This pair evolves together in the compartment, as seen from panel b) to

panel e). The vertical highlighters act to separate different pairs of density patches, because forward-time repellers serve as boundaries to the regions where the scalar patch moves coherently. In other words, the scalar patches on the left and right of one vertical structure are going to separate over time. Panels c) and f) show the backward-time FTLE with the density iso-contour. The structures are predominantly aligned with the IGW. Note that the backward-time FTLE correspond to the attractors; hence, these newly developed vertical structures act to hold together the pairs of patches identified in the forward-time FTLE compartments. To aid in the interpretation of the LCS, which acts as organizers for the plasma blob evolution, we focus on the pair of blobs shown in panels a) and d). In panel a), this patch is still connected with the red wave phase at the bottom right of the panel. The emergence of the vertical structures in panel b) indicates that on the left and right of this pair, separated by the solid red lines in panel a) and d), motion will be different from the evolution of this pair. By examining the pair of patches to the left and right, we observe that the rotation of the pairs is different. The more complicated vertical structures that are seen in panel d) indicate that the motion will be even more complicated in future times. In addition to the separating structures, the emergence of attracting structures, as indicated by the solid black line in panel d), act to hold the pair together; so, there is not much difference in the coherent motion within the pair. As such, we conclude that during the overturning event, the plasma flow develops separated compartments, in which pairs of density patches evolve together. As LCS techniques help to identify important features on the plasma density evolution, they become useful in the extraction of plasma fronts and other scintillation producing irregularities that may affect operational communication, navigation and imaging systems.

5. Summary and challenges

Turbulent hydrodynamic mixing, induced by the Rayleigh–Taylor (RT) instabilities, occurs in settings as varied as exploding stars (supernovae), inertial confinement fusion (ICF) and macroscopic flows in fluid dynamics, such as ionospheric plasmas. In this paper, we reviewed physics-based predictive modeling and novel multi-nesting computational techniques that were developed in order to characterize strongly inhomogeneous non-Kolmogorov ionospheric media. Nested numerical simulations of ionospheric plasma density structures, associated with the nonlinear evolution of the primary and secondary Rayleigh–Taylor instabilities in the Equatorial Spread F (ESF), were presented. For the limited domain and nested simulations, the lateral boundary conditions were treated via implicit relaxation techniques that were applied in buffer zones in which the density of the charged particles for each nest was relaxed to equal the density of the charged particles obtained from the parent domain. The high resolution in the targeted regions offered by the nested model is able to resolve the scintillation producing ionospheric irregularities that are associated with secondary RT instabilities, characterized by sharp gradients of

the refractive index at the edges of the mixed regions ([58]). In [99] and [100], our studies focused on the charge-neutral interactions and the statistics that are associated with the stochastic Lagrangian motion. We examined the organizing mixing patterns for the plasma flows, which occur due to polarized gravity wave excitations in the neutral field, using Lagrangian coherent structures (LCS). LCS objectively depict the flow topology, and the extracted scintillation producing irregularities indicate a generation of ionospheric density gradients, due to the accumulation of plasma. The scintillation effects that are induced by the trapping of the electromagnetic (EM) waves in the parabolic cavities, created by the refractive index gradients along the propagation paths, were analyzed in [54], [57] and [68].

The ionosphere plays a major role in space sciences due to its important influence on the propagation of electromagnetic (EM) waves (radio waves, microwaves and lasers). High-impact ionospheric environments can significantly impact communication, navigation and imaging systems, primarily through the development of electron density irregularities and plasma turbulence, which often occurs in the vicinity of large electron density gradients. Associated irregularities and inhomogeneous, anisotropic, non-Kolmogorov and patchy ionospheric dynamics can have a spatial range from tens of kilometers through meter scales. A wide variety of physical processes occur on these disparate scales, and this has posed a considerable challenge to the goal of a truly self-consistent, comprehensive model-based understanding of irregularity dynamics and morphology. Recent studies have demonstrated the importance of a full 3D, high resolution nested approach to the local studies of limited-area ionospheric environments and for understanding the impact of mesoscale and small-scale ionospheric processes on EM propagation ([44, 45, 57, 58, 68–70, 99, 100]).

Acknowledgments

References

[1] Abarzhi S I 2010 Review of theoretical modeling approaches of Rayleigh–Taylor instabilities and turbulent mixing *Phil. Trans. R. Soc.* A **368** 1809–28

[2] Abarzhi S I 2008 Coherent structures and pattern formation in the Rayleigh–Taylor turbulent mixing *Phys. Scr.* **78** 015401

[3] Abarzhi S I and Rosner R 2010 Comparative study of approaches for modeling Rayleigh–Taylor turbulent mixing *Phys. Scr.* **T142** 1–12

[4] Alam K, de Paula E R and Bertoni F C P 2004 Effects of the fringe field of Rayleigh–Taylor instability in the equatorial E and valley regions *J. Geophys. Res.* **109** 12310

[5] Aveiro H C, Hysell D L, Caton R G, Groves K M, Klenzing J, Pfaff R F, Stoneback R and Heelis R A 2012 *J. Geophys. Res.* **117** A03325

[6] Basu S and Basu S 1976 Correlated measurements of scintillations and *in situ* F-region irregularities *Geophys. Res. Lett.* **3** 681–4

[7] Basu S, Basu S, Aarons J, McClure J P and Cousins M D 1978 On the coexistence of kilometer- and meter-scale irregularities in the nighttime equatorial F region *J. Geophys. Res.* **83** 4219

[8] Behrens J 2005 Adaptive atmospheric modeling: scientific computing at its best *Comput. Sci. Eng.* **7** 76–83

[9] Berkner L V and Wells H W 1934 F region ionosphere -investigation at low latitudes *Terres. Magn.* **39** 215

[10] Davies H C 1983 Limitations of some common lateral boundary schemes used in regional NWP models *Mon. Wea. Rev.* **111** 1002–12

[11] de La Beaujardiere O 2004 C/NOFS: a mission to forecast scintillations *J. Atmos. Sol.-Terr. Phys.* **66** 1573–91

[12] de Boer J D, Noel A and Maurice J-P S 2010 The effects of mesoscale regions of precipitation on the ionospheric dynamics, electrodynamics and electron density in the presence of strong ambient electric field *Ann. Geophys.* **28** 1345–60

[13] Cheng B and Mahalov A 2013 Euler equations on a fast rotating sphere–time-averages and zonal flows *Eur. J. Mech.* B **37** 48–58

[14] Dickinson R E, Ridley E C and Roble R G 1981 A three dimensional, time dependent general circulation model of the thermosphere *J. Geophys. Res.* **86** 1499–512

[15] Dietachmayer G S and Droegemeier K K 1992 Application of continuous dynamic grid adaptation techniques to meteorological modeling, Part I *Mon. Wea. Rev.* **120** 1675–706

[16] Durazo J, Kostelich E, Mahalov A and Tang W 2014 Assessing a local ensemble transform Kalman filter: observing system experiments with an ionospheric model submitted for publication

[17] Fejer B G and Kelley M C 1980 Ionospheric irregularities *Rev. Geophys.* **18** 401

[18] Fesen C G, Crowley R G, Roble R G, Richmond A D and Fejer B G 2000 Simulation of the pre-reversal enhancement in the low latitude vertical ion drifts *Geophys. Res. Lett.* **27** 1851

[19] Flandoli F and Mahalov A 2012 Stochastic 3D rotating Navier–Stokes equations: averaging, convergence and regularity *Arch. Ration. Mech. Anal.* **205** 195–237

[20] Fuller-Rowell T J 1984 A two dimensional, high resolution, nested-grid model of the thermosphere 1, Neutral response to an electric field 'spike *J. Geophys. Res.* **89** 2971–90

[21] Fuller-Rowell T J 1985 A two dimensional, high resolution, nested-grid model of the thermosphere 2, Response of the thermosphere to narrow and broad electrodynamics features *J. Geophys. Res.* **90** 6567–86

[22] Fuller-Rowell T J and Rees D A 1980 A three dimensional time dependent global model of the thermosphere *J. Atmos. Sci.* **37** 2545–67

[23] Fuller-Rowell T J, Rees D, Quegan S, Moffett R J and Bailey G J 1987 Interactions between neutral thermospheric composition and the polar ionosphere using a coupled ionosphere–thermosphere model, *J. Geophys. Res.* **92** 7744–8

[24] Galperin B, Sukoriansky S, Dikovskaya N, Read P L, Yamazaki Y H and Wordsworth R 2006 Anisotropic turbulence and zonal jets in rotating flows *Nonlin. Process. Geophys.* **13** 83–98

[25] Glimm J, Grove J W, Li X L and Tan D C 2000 Robust computational algorithms for dynamic interface tracking in three dimensions *SIAM J. Sci. Comput.* **21** 2240–56

[26] Heelis R A, Lowell J K and Spiro R W 1982 A model of the high-latitude ionospheric convection pattern *J. Geophys. Res.* **87** 6339–45

[27] Herrmann M and Blanquart G 2006 Flux corrected finite volume scheme for preserving scalar boundedness in reacting large-eddy simulations *AIAA J.* **44** 12

[28] Hodur R M 1997 The naval research laboratory coupled ocean/atmosphere mesoscale prediction system (COAMPS) *Mon. Wea. Rev.* **125** 1414–30

[29] Huang C S and Kelley M C 1996a Nonlinear evolution of equatorial spread F, 2. Gravity wave seeding of Rayleigh–Taylor instability *J. Geophys. Res.* **101** 293–302

[30] Huang C S and Kelley M C 1996b Nonlinear evolution of equatorial spread F, 4. gravity waves, velocity shear and day-to-day variability *J. Geophys. Res.* **101** 24521–32

[31] Huba J D, Joyce G and Fedder J 2009 Sami2 is another model of the ionosphere (SAMI2): a new low-latitude ionosphere model *J. Geophys. Res.* **105** 23035–53

[32] Huba J D, Joyce G, Krall J and Fedder J 2009 Ion and electron temperature evolution during equatorial spread-F *Geophys. Res. Lett.* **36** L15102

[33] Huba J D, Krall J and Joyce G 2009 Atomic and molecular ion dynamics during equatorial spread-F *Geophys. Res. Lett.* **36** L10106

[34] Huba J D, Ossakow S L, Joyce G, Krall J and England S L 2009 Three-dimensional equatorial spread F modeling: zonal neutral wind effects *Geophys. Res. Lett.* **36** L19106

[35] Hunt J C R, Pacheco J R, Mahalov A and Fernando H J S 2005 Effects of rotation and sloping terrain on fronts of density currents *J. Fluid Mech.* **537** 285–315

[36] Hysell D L and Burcham J D 2000 The 30 MHZ radar interferometer studies of midlatitude E-region irregularities *J. Geophys. Res.* **105** 797

[37] Hysell D L, Larsen M F and Zhou Q H 2004 Common volume coherent and incoherent scatter radar observations of midlatitude sporadic E layers and QP echoes *Ann. Geophys.* **22** 3277–90

[38] Hysell D L, Yamamoto M and Fukao S 2002 Simulation of plasma clouds in the midlatitude E-region ionosphere with implications for Type 1 and Type 2 quasi-periodic echoes *J. Geophys. Res.* **107** 1313

[39] Hysell D L, Rodrigues F S, Chau J L and Huba J D 2008 Full profile incoherent scatter analysis at Jicamarca *Ann. Geophys.* **26** 59

[40] Hysell D L 2008 30 MHz radar observations of artificial E region field-aligned plasma irregularities *Ann. Geophys.* **26** 117

[41] Hysell D L, Hedden R B, Chau J L, Galindo F R, Roddy P A and Pfaff R F 2009 Comparing F region ionospheric irregularity observations from C/NOFS and Jicamarca *Geophys. Res. Lett.* doi:10.1029/2009GL038983

[42] Jiang G-S and Peng D 2000 Weighted ENO schemes for Hamilton Jacobi equations *SIAM J. Sci. Comput.* **21** 2126–43

[43] Joseph B, Mahalov A, Nicolaenko B and Tse K L 2004 Variability of turbulence and its outer scales in a model tropopause jet *J. Atmos. Sci.* **61** 621–43

[44] Jung C Y and Mahalov A 2010 Wave propagation in random waveguides *Discrete Contin. Dynam. Syst.* **28** 147–59

[45] Jung C Y, Kwon B, Mahalov A and Nguyen T B 2013 Maxwell solutions in media with multiple random interfaces *Int. J. Num. Anal. Model.* **11** 193–213

[46] Keskinen M I and Ossakow S I 1981 On the spatial power spectrum of the E B gradient drift instability in ionospheric plasma clouds *J. Geophys. Res.* **86** 6987

[47] Killeen T L 1987 Energetics of the Earth's thermosphere *Rev. Geophys.* **25** 433–54

[48] Killeen T L and Roble R G 1988 Thermosphere dynamics: contributions from the first five years of the dynamics explorer program *Rev. Geophys.* **26** 329–67

[49] Kelley M C, Larson M F, La Hoz C and McClure J P 1981 Gravity wave initiation of equatorial spread F: A case study *J. Geophys. Res.* **86** 9087

[50] Kelley M C 2009 *Earth's Ionosphere, Plasma Physics and Electrodynamics* (Amsterdam: Elsevier)

[51] Korotkova O, Farwell N and Mahalov A 2009 Effects of the jet-stream on the intensity of laser beams propagating along slanted paths in the upper layers of the turbulent atmosphere *Waves Random Complex Media* **19** 692–702

[52] Krall J, Huba J D, Joyce G and Zalesak S T 2009 Three-dimensional simulation of equatorial spread-F with meridional wind effects *Ann. Geophys.* **27** 1821–30

[53] Krall J, Huba J D and Martinis C 2010 Density enhancements associated with equatorial spread F *Ann. Geophys.* **28** 327–37

[54] Krattenthaler C, Kryuchkov S, Mahalov A and Suslov S 2013 On the problem of electromagnetic field quantization *Int. J. Theor. Phys.* **52** 4445–60

[55] Lehmann R 1993 On the choice of relaxation coefficients for Davies lateral boundary scheme for regional weather prediction models *Meteor. Atmos. Phys.* **52** 1–14

[56] Mahalov A, Moustaoui M and Nichols B 2008 Three-dimensional instabilities in non-parallel shear stratified flows *Kinetic Related Models* **2** 215–29

[57] Mahalov A and Suslov S 2013 Solution of parabolic wave equation for inhomogeneous media in linear and quadratic approximation *Proc. Am. Math. Soc.* at press

[58] Mahalov A and Moustaoui M 2013 Multiscale nested simulations of Rayleigh–Taylor instabilities in ionospheric flows *J. Fluids Eng.* **136**

[59] Mahalov A and Moustaoui M 2009 Vertically nested nonhydrostatic model for multi-scale resolution of flows in the upper troposphere and lower stratosphere *J. Comput. Phys.* **228** 1294–311

[60] Mahalov A and Moustaoui M 2010 Characterization of atmospheric optical turbulence for laser propagation *Laser Photon. Rev.* **4** 144–59

[61] Mahalov A, Lefevre R and Cocks S 2009 Lasers and applications in science and engineering. atmospheric propagation of electromagnetic waves *Int. Soc. Opt. Eng.* **7200** 72000A-10

[62] Mahalov A, Moustaoui M and Nichols B 2007 Computational studies of inertia-gravity waves radiated from upper tropospheric Jets *J. Theor. Comput. Fluid Dynamics* **21** 399–422

[63] Mahalov A, Joseph B, Nicolaenko B and Tse K L 2004 Eddy-mixing in jet-stream turbulence under stronger stratification *Geophys. Res. Lett.* **23** L23111–5

[64] Mahalov A and Moustaoui M 2012 Multiscale nesting and high performance computing simulations of limited area atmospheric environments, *Handbook of Environmental Fluid Dynamics* vol 2 (Abingdon: Taylor and Francis) pp 301–11

[65] Mahalov A, Nicolaenko B and Zhou Y 1998 Energy spectra of strongly stratified and rotating turbulence *Phys. Rev. E* **57** 6187–90

[66] Mahalov A 2009 Atmospheric characterization and ensemble forecasting of multi-scale flows in the upper troposphere and lower stratosphere (UTLS) *AIAA 2009–110* (Reston, VA: American Institute of Aeronautics and Astronautics) pp 1–6 (invited paper)

[67] Mahalov A, Pacheco J R, Fernando H J S and Hunt J C R 2000 Effects of rotation on fronts of density currents *Phys. Lett.* A **270** 149–56

[68] Mahalov A, Suazo E and Suslov S 2013 Spiral laser beams in inhomogeneous media *Opt. Lett.* **38** 2763–9

[69] Mahalov A and Suslov S 2012 An 'Airy Gun': self-accelerating solutions of the time-dependent Schrodinger equation *Phys. Lett.* A **377** 33–8

[70] Mahalov A and Suslov S 2013 Wigner function approach to oscillating solutions of the nonlinear Schrodinger equation *J. Nonlin. Opt. Phys. Mater.* **22** 1350013

[71] Marbaix P H, Gallee O, Brasseur J P and Ypersele V 2003 Lateral boundary conditions in regional climate models: a detailed study of the relaxation procedure *Mon. Wea. Rev.* **111** 461–79

[72] Maruyama T, Saito S, Kawamura M, Nozaki K, Krall J and Huba J D 2009 Equinoctial asymmetry of a low-latitude ionosphere-thermosphere system and equatorial irregularities: evidence for meridional wind control *Ann. Geophys.* **27** 2027–34

[73] Moustaoui M, Mahalov A and Kostelich E 2014 A numerical method based on leapfrog and a fourth order implicit time filter *Mon. Weather Rev.* at press accepted for publication

[74] Oddo P and Pinardi N 2008 Lateral open boundary conditions for nested limited area models: a scale selective approach *Ocean Modeling* **10** 134–56

[75] Ossakow S L 1981 Spread F theories: a review *J. Atmos. Terr. Phys.* **43** 437–52

[76] Ossakow S L and Chaturvedi P K 1978 Morphological studies of rising equatorial spread F bubbles *J. Geophys. Res.* **83** 2085–90

[77] Oya H, Takahashi T and Watanabe S 1986 Observation of low latitude ionosphere by the impedance probe on board the Hinotori satellite *J. Geomag. Geoelectr.* **38** 111–23

[78] Oyama K-I, Schlegel K and Watanabe S 1988 Temperature structure of plasma bubbles in the low latitude ionosphere around 600 km altitude *Planet. Space Sci.* **36** 553–67

[79] Park J, Min K W, Kim V P, Kil H, Su S-Y, Chao C K and Lee J-J 2008a Equatorial plasma bubbles with enhanced ion and electron temperatures *J. Geophys. Res.* **113** A09318

[80] Park J, Stolle C, Luhr H, Rother M, Su S-Y, Min K W and Lee J-J 2008b Magnetic signatures and conjugate features of low-latitude plasma blobs as observed by the CHAMP satellite *J. Geophys. Res.* **113** A09313

[81] Prolls G W 1981 Latitudinal structure and extension of the polar atmospheric disturbance *J. Geophys. Res.* **86** 2385–8

[82] Raghavarao R, Sekar R and Suhasini R 1992 Nonlinear numerical simulation of equatorial spread f: effects of winds and electric fields *Adv. Space Res.* **12** 227–30

[83] Retterer J M 2010 Forecasting low-latitude radio scintillation with 3D ionospheric plume models: 1. Plume model *J. Geophys. Res.* **115** A03306

[84] Retterer J M 2010 Forecasting low-latitude radio scintillation with 3D ionospheric plume models: 2. Scintillation calculation *J. Geophys. Res.* **115** A03307

[85] Retterer J M 2005 Physics-based forecasts of equatorial radio scintillations for the C/NOFS *Space Weather* **3** S12C03

[86] Roble R G and Ridley E C 1994 A thermosphere–ionosphere–mesosphere electrodynamics general circulations model (time-GCM): Equinox solar cycle minimum simulations (30–500 km) *Geophys. Res. Lett.* **21** 417–20

[87] Scannapieco A J and Ossakow S L 1976 Nonlinear equatorial spread F *Geophys. Res. Lett.* **3** 451–4

[88] Schunk R W and Nagy A E 2000 Ionospheres: physics *Plasma Physics and Chemistry* (Cambridge: Cambridge University Press)

[89] Sekar R, Suhasini R and Raghavarao R 1994 Effects of vertical winds and electric fields in the nonlinear evolution of equatorial spread F *J. Geophys. Res.* **99** 2205–13

[90] Sekar R and Kherani E A 2002 Effects of molecular ions on the collisional Rayleigh–Taylor instability: nonlinear evolution *J. Geophys. Res.* **107** 1–9

[91] Shchepetkin A and McWilliams J C 2005 Regional ocean model system: a split-explicit ocean model with a free surface and topography-following vertical coordinate *Ocean Modeling* **9** 347–404

[92] Skamarock W C and Klemp J B 2008 A time-split nonhydrostatic atmospheric model for weather research and forecasting applications *J. Comput. Phys.* **227** 3465–85

[93] Skamarock W C and Klemp J B 1993 Adaptive grid refinement for two-dimensional and three-dimensional

nonhydrostatic atmospheric flow *Mon. Wea. Rev.* **121** 788–804

[94] Smolarkiewicz P K and Grell G A 1992 A class of monotone interpolation schemes *J. Comp. Phys.* **101** 431–40

[95] Sreenivasan K R and Abarzhi S I 2013 Acceleration and turbulence in Rayleigh–Taylor mixing *Phil. Trans. R. Soc. A* **371** 20130167

[96] Steenburgh R A, Smithtro C G and Groves K M 2008 Ionospheric scintillation effects on single frequency GPS *Space Weather* **6** S04D02

[97] Sun Z P, Turco R P and Walterscheid R L 1995 Thermospheric response to morning diffuse aurora: high resolution three-dimensional simulations *J. Geophys. Res.* **100** 23779–93

[98] Sutton R T, Maclean H, Swinbank R, ONeill A and Taylor F W 1994 High resolution stratospheric tracer fields estimated from satellite observations using lagrangian trajectory calculations *J. Atmos. Sci.* **51** 29953005

[99] Tang W and Mahalov A 2013 Stochastic Lagrangian dynmics for charged flows in the E-F regions of ionosphere *Physics of Plasmas* **20** 032305.1–032305.12

[100] Tang W and Mahalov A 2014 The response of plasma density to breaking inertial gravity waves in the lower region of ionosphere *Physics of Plasmas* **21** 042901

[101] Tatarskii V I, Ishimaru A and Zavorotny V U (ed) 1993 *Wave Propagation in Random Media (Scintillation)* (SPIE Optical Engineering Press)

[102] Taur R R 1976 Simulations 1.5 GHz and 4 GHz ionospheric scintillation measurements *Radio Sci.* **11** 1029–36

[103] Tse K-L, Mahalov A, Nicolaenko B and Fernando H J S 2003 Quasi-equilibrium dynamics of shear-stratified turbulence in a model tropospheric jet *J. Fluid Mech.* **496** 73–103

[104] Tsunoda R T 1988 High-latitude F-region irregularities: a review and synthesis *Rev. Geophys.* **26** 719–60

[105] Tsunoda R T 1983 On the generation and growth of equatorial backscatter plume structuring of the westwalls of upwelling *J. Geophys. Res.* **88** 4869

[106] Tsynkov S V 2009 On SAR imaging through the Earth's ionosphere *SIAM J. Imaging Sci.* **2** 140–62

[107] Vadas S L and Liu H-L 2009 The generation of large-scale gravity waves and neutral winds in the thermosphere from the dissipation of convectively-generated gravity waves *J. Geophys. Res.* **114** A10310

[108] Watanabe S and Oya H 1986 Occurence characteristics of low latitude ionosphere irregularities observed by impedance probe on board the Hinotori satellite *J. Geomag. Geoelectr.* **38** 125–49

[109] Wicker L J and Skamarock W C 2002 Time splitting methods for elastic models using forward time schemes *Mon. Wea. Rev.* **130** 2088–97

[110] Woodman R F and La Hoz C 1976 Radar observation of F region equatorial irregularities *Geophys Res.* **81** 5447

[111] Xu Z W, Wu J and Wu Z S 2004 A survey of ionospheric effects on space-based radar *Waves Random Complex Media* **14** S189–273

[112] Yokoyama T, Su S-Y and Fukao S 2007 Plasma blobs and irregularities concurrently observed by ROCSAT-1 and equatorial atmosphere radar *J. Geophys. Res.* **112** A05311

[113] Yokoyama T, Horinouchi T, Yamomoto M and Fukao S 2004 Modulation of the midlatitude ionospheric E region by atmospheric gravity waves through polarization electric field *J. Geophys. Res.* **109** A12307

[114] Yokoyama T, Yamomoto M and Fukao S 2004 Three-dimensional simulation on generation of polarization electric field in the midlatitude E-region ionosphere *J. Geophys. Res.* **109** A01309

[115] Yokoyama T, Otsuka Y, Ogawa T, Yamomoto M and Hysell D L 2008 First three-dimensional simulation of the Perkins instability in the nighttime midlatitude ionosphere *Geophys. Res. Lett.* **35** L03101

[116] Yokoyama T, Yamomoto M and Fukao S 2003 Computer simulation of polarization electric field as a source of midlatitude field-aligned irregularities *J. Geophys. Res.* **108** 1054

[117] Yokoyama T, Yamomoto M and Fukao S 2009 Three-dimensional simulation on generation of polarization electric field in the midlatitude E-region ionosphere *J. Geophys. Res.* **109** A01309

[118] Yokoyama T, Hysell D L, Otsuka Y, Ogawa T and Yamomoto M 2009 Three-dimensional simulation of the Perkins Es-layer instabilities in the nighttime midlatitude ionosphere *J. Geophys. Res.* **114** A03308

[119] Yokoyama T and Hysell D L 2010 A new midlatitude ionosphere electrodynamics coupling model (MIEGO): latitudinal dependence and propagation of medium-scale traveling ionopsheric disturbances *Geophys. Res. Lett.* **37** L08105

[120] Zalesak S T 1979 Fully multidimensional flux-corrected transport algorithms for fluids *J. Comput. Phys.* **31** 335–62

[121] Wolf E 2007 *Introduction to Theories of Coherence and Polarization of Light* (Cambridge: Cambridge University Press)

[122] Zhou Y *et al* 2003 Progress in understanding turbulent mixing induced by Rayleigh–Taylor and Richtmyer–Meshkov instabilities *Phys. Plasmas* **10** 1883